

Physics of melt extraction from the mantle: speed and style

Richard F. Katz,¹ David W. Rees Jones², John F. Rudge³ and Tobias Keller,^{4,5}

¹Department of Earth Sciences, University of Oxford, Oxford, UK, OX2 6NA; email: richard.katz@earth.ox.ac.uk

²School of Mathematics and Statistics, University of St Andrews, St Andrews, KY16 9SS, United Kingdom

³Bullard Laboratories, Department of Earth Sciences, University of Cambridge, Madingley Road, Cambridge, CB3 0EZ, UK.

⁴School of Geographical & Earth Sciences, University of Glasgow, Glasgow, G12 8QQ, United Kingdom

⁵Institute of Geochemistry & Petrology, ETH Zürich, 8092 Zürich, Switzerland

Xxxx. Xxx. Xxx. Xxx. YYYY. AA:1–35

This article's doi:
10.1146/((please add article doi))

Copyright © YYYY by Annual Reviews.
All rights reserved

Keywords

magma, asthenosphere, rheology, partial melting, channelization, dunite, rock microstructure, mid-ocean ridge, subduction, OTHERS?

Abstract

Melt extraction from the partially molten mantle is among the fundamental processes shaping the solid Earth today and over geological time. A diversity of properties and mechanisms contribute to the physics of melt extraction. We review progress of the past ~25 years of research in this area, with a focus on understanding the speed and style of buoyancy-driven melt extraction. Observations of U-series disequilibria in young lavas and the surge of deglacial volcanism in Iceland suggest this speed is rapid compared to that predicted by the null hypothesis of diffuse porous flow. The discrepancy indicates that the style of extraction is channelised. We discuss how channelisation is sensitive to mechanical and thermochemical properties and feedbacks, and to asthenospheric heterogeneity. We review the grain-scale physics that underpins these properties and hence determines the physical behavior at much larger scales. We discuss how the speed of melt extraction is crucial to predicting the magmatic response to glacial and sea-level variations. We assess the frontier of current research and identify fertile where significant advances are expected over the next 25 years. In particular, we highlight the coupling of melt extraction with more realistic models of mantle thermochemistry and rheological properties. These will be crucial in understanding petrologically complex settings such as subduction zones.

Contents

1. INTRODUCTION	2
2. PHYSICS OF MELT EXTRACTION IN THE LABORATORY	3
2.1. Permeability	4
2.2. Viscosity	5
2.3. The compaction length	7
2.4. Reactive melting and channelization in the laboratory	8
3. PHYSICS OF MELT EXTRACTION IN THE ASTHENOSPHERE	9
3.1. Observational proxies of magma speed	10
3.2. Mechanisms of flow channelisation	11
3.3. Climate cycles, sea level & magmatism	21
4. CURRENT FRONTIERS OF RESEARCH	24
4.1. Subduction-zone magmatism	24
4.2. Ascent through brittle fracture	25
4.3. Melt at the LAB and in the lithosphere	26
4.4. Coupling petrological thermodynamics	27

1. INTRODUCTION

Melting occurs when the internal energy of a crystalline solid is sufficient to break lattice bonds, creating disorder at the molecular scale. The melt therefore has higher entropy and higher enthalpy than its solid residue; it typically also has a different equilibrium composition. These differences confer a lower viscosity and, in general, a distinct density. In the presence of a gravitational potential, melt segregates from its residue if a permeable pathway is available. That segregation, which occurs at the grain scale, transports heat and chemistry over much larger scales. Indeed, melt segregation creates planetary radial structure, creates and destroys chemical heterogeneity, cools the interior and shapes the surface and atmosphere.

On Earth, these processes are manifest in close association with plate tectonics and mantle convection. Indeed magmatism is generally discussed in terms that are specific to a tectonic context (e.g., spreading centres, subduction zones and intraplate hot-spot volcanoes). The presence of basaltic volcanism in each of these settings provides clear evidence that at least some of the magma is derived from mantle melting. For each tectonic context, there are a variety of geographical instances where observations are made. This data raises questions that pertain both to local characteristics and global systematics. A question general enough to apply to all settings and to physics from the scale of grains to that of tectonic plates is as follows: *What is the speed and style of melt extraction from where it is produced in the asthenospheric mantle to where it interacts with the lithosphere?* The present review is organised around this question and investigates the physical processes it evokes.

The simplest, null hypothesis for the style of melt transport is diffuse porous flow. This states that melt produced at the grain scale is transported through a permeable network of melt tubules (pores) along the junctions between grains. This hypothesis also states that porosity is diffuse, i.e., that it varies slowly in space and time. In this context, the gravitational body force, acting on the density difference between solid and liquid $\Delta\rho = \rho_s - \rho_\ell$ (typically positive), drives segregation. A balance between this buoyancy force and

Porosity, ϕ : the volume fraction of melt in a control volume that contains many grains and pores. Equivalent to the melt fraction.

the viscous drag force associated with Darcian porous flow leads to a characteristic melt speed (sometimes called the *percolation velocity*) of

$$w_0 = \frac{k\Delta\rho g}{\phi\mu}, \quad (1)$$

where g is the magnitude of gravitational acceleration, μ is the dynamic viscosity of the liquid, and k is the permeability, a function of the grain size and porosity, discussed below. A typical value of w_0 for conditions in partially molten regions of the upper mantle is probably in the range of 0.01–1 m/yr. Proxies for melt speed discussed below, however, indicate speeds in the range 1–100 m/yr. Here and in previous work, this difference has been attributed to a style of flow that is channelised, rather than diffuse. The present review is mostly concerned with the causes and consequences of flow localisation into channels.

The poro-viscous, continuum theory underlying our discussion of partially molten rock was published by McKenzie (1984) (see also Fowler 1984). Its broad physical basis and key applications were reviewed in Stevenson & Scott (1991); Kohlstedt & Zimmerman (1996) discussed the physics with a focus on rheological properties. A recent book provides a comprehensive and didactic treatment (Katz 2021). And while the percolation velocity was noted by earlier workers, McKenzie (1984) recognised a natural length scale of magma–mantle interaction. This *compaction length*, discussed in sec. 2.3, is closely related to the dimensions of emergent flow localisation, porosity waves, and boundary layers.

Our focus in this review is on the physical mechanisms that account for the discrepancy in melt-transport speed between diffuse porous flow and inferences from observational proxies. We build on the landmark review of Kelemen et al. (1997) and trace forward some of the themes identified there. Within the limited space of this review, we mostly cite literature published after Kelemen et al. (1997); references to earlier work are in the cited publications. In section 2, we review physics at the grain and laboratory scales that underpins continuum theories at larger scales. We highlight experiments that demonstrate the link between reactive melting and channelised melt flow. In section 3, we review two observational proxies for magma speed. We then discuss a family of physics-based models of channelised flow. In section 3.3 we discuss the hypothesis that sea level modulates submarine magmatism. In section 4, we scan the horizon of current research to identify themes and ideas that may form the basis of discoveries in the next 25 years. We conclude with a summary and list of outstanding questions to motivate future research.

2. PHYSICS OF MELT EXTRACTION IN THE LABORATORY

Mantle partial melting is dispersed at the grain scale, where juxtaposition of different minerals leads to eutectic-like solidus lowering. In the absence of significant deviatoric stress, the solid–liquid microstructure that forms is controlled by surface energy. The system tends to a state of textural equilibrium, where the energy bound up in solid–liquid and solid–solid interfaces is minimised. For mantle rocks, the low surface energy of the solid–liquid interface stabilises an interconnected pore network distributed between grains.

How fast is textural equilibrium established? In laboratory experiments textural equilibrium is reached in a matter of hours, but such experiments have much finer grain sizes than the mantle. If the rate of textural equilibration of a pore is limited by diffusion within the melt phase, then the equilibration time τ is expected to scale as the cube of pore size L , $\tau = L^3/K$, with a prefactor K that depends on temperature. For a typical mantle

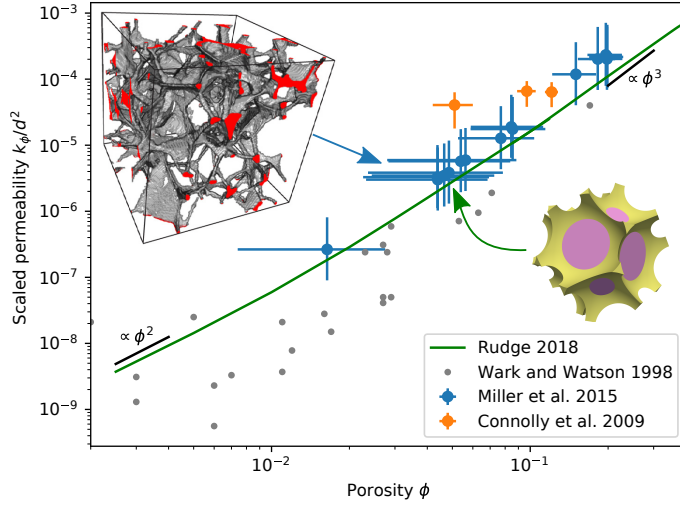


Figure 1

Scaled permeability (permeability k divided by the square of grain size d) plotted against porosity ϕ for a selection of experimental and theoretical studies. Shown are i) textural equilibrium model of identical truncated octahedral grains with a dihedral angle of 40° , adapted from Rudge (2018a) (CC BY 4.0). The geometry is illustrated in the bottom right with melt network in yellow, grain in pink, with a porosity of 5%; ii) rock-analogue experimental measurements on synthetic quartzites from Wark & Watson (1998); iii) Stokes-flow calculations of permeability using X-ray microtomography of the pore space of olivine + basalt samples from Miller et al. (2015). Top left shows a microtomography image for a porosity of 5%, adapted from Miller et al. (2014). Scaled permeability shown assumes an average grain size of $35^{+25}_{-15} \mu\text{m}$ for all experiments (similar to those quoted in Miller et al. (2014)); iv) high-pressure, high-temperature centrifuge experiments on olivine + basalt samples by Connolly et al. (2009); v) Short black lines show the expected slopes on this plot for $k \propto d^2 \phi^2$ and $k \propto d^2 \phi^3$. For porosity less than 2%, the textural-equilibrium permeability can be well-approximated by $k = d^2 \phi^2 / 1600$ (von Bargen & Waff 1986; Rudge 2018a); for porosity greater than 10%, well-approximated as $k = d^2 \phi^3 / 75$.

grain size $d \sim 3 \text{ mm}$, and a porosity of $\phi \sim 0.1\%$, the pore size $L = d\sqrt{\phi} \sim 100 \mu\text{m}$. An experimentally estimated value of $K \sim 10^{-21} \text{ m}^3 \text{ s}^{-1}$ (Holness & Siklos 2000) yields an equilibration time $\tau \sim 30$ years.

Liquid–solid interaction at the grain scale ($\leq \text{mm}$) has consequences at the continuum scale ($\geq \text{m}$ to km). Laboratory experiments provide a means to measure and understand the physics of this interaction, and a basis for deriving constitutive laws to be used in continuum models. This section reviews laboratory experiments and how the relevant physics has been quantitatively upscaled.

2.1. Permeability

The key material property for understanding melt migration is the permeability of the partially molten rock. This depends on the size d of the mineral grains, the porosity ϕ of the rock and, importantly, on the geometrical details of how the melt is arranged at the grain scale (i.e., on the microstructure). Typically permeability is described by a semi-empirical law of the form $k = d^2 \phi^n / C$, where n is an exponent between 2 and 3, and C is

a numerical prefactor.

Different approaches have been taken to estimating permeability, and some recent estimates are shown in **Figure 1**. One approach is to assume a particular geometry for the melt network, and then calculate the permeability by solving a Stokes flow problem for melt flow at the pore scale. Rudge (2018a) presents an example of this approach, where a textural-equilibrium geometry for a collection of identical, truncated, octahedral grains is assumed (**Figure 1**). At small porosity, the melt forms a connected network of tubes along the grain edges and the permeability scales as $k \propto d^2 \phi^2$. As porosity increases, more of the grain faces become wetted and the permeability transitions to scaling as $k \propto d^2 \phi^3$.

The textural-equilibrium geometry model of Rudge (2018a), shown in **Figure 1**, is highly idealised and does not account for the heterogeneity of grain size and type seen in real rocks. To quantify the effect of this heterogeneity, Miller et al. (2014, 2015) have recently estimated the permeabilities of olivine + basalt samples by microtomographic imaging of the pore space (**Figure 1b**), followed by Stokes flow calculation of permeability. Their results are broadly consistent with the idealized, theoretical estimates.

There have been several experimental efforts to directly measure the permeability of rock samples by measuring the rate of fluid flow in response to an applied pressure gradient. **Figure 1c** includes experimental results from Wark & Watson (1998), who studied synthetic quartzite as a rock analogue, and Connolly et al. (2009), who studied olivine + basalt samples. These experiments are broadly in line with the simple textural equilibrium models.

2.2. Viscosity

Crucial to any geodynamic model of melt extraction is an understanding of how the skeleton of solid mineral grains resists deformation. This resistance is described by two viscosities: a shear viscosity η , and a compaction viscosity ζ . The shear viscosity relates the deviatoric stress and deviatoric strain rate, just as for a pure solid material. The compaction viscosity is a two-phase flow concept and describes resistance to the closing or opening of pore space due to a difference in pressure between the solid and the melt.

Figure 2 plots estimates of the compaction and shear viscosity as a function of porosity ϕ for both micromechanical models and laboratory experiments. One of the simplest micromechanical models, adopted by many authors (e.g., Scott & Stevenson 1986; Sleep 1988; Bercovici et al. 2001; Hewitt & Fowler 2008; Simpson et al. 2010a,b; Schmeling et al. 2012), is to assume the skeleton of grains acts like a uniform viscous fluid with shear viscosity η_s . For small porosity, these models imply $\eta \sim \eta_s(1 - \phi)$ and $\zeta \sim D\eta_s/\phi$ where D is an $O(1)$ geometrical prefactor. However, a uniform-viscous-fluid model fails to capture the true physics at the grain scale, which involves the motion of lattice defects, and sliding, plating, and diffusion along grain boundaries (Kohlstedt & Hansen 2015). Such grain-scale physics can be upscaled to produce continua with a macroscale viscous rheology; the resulting compaction and shear viscosities as a function of porosity are quite different from models which assume a grain-scale viscous rheology. **Figure 2** shows model viscosities for Coble creep (grain-boundary diffusion creep, similar to the models of Cooper & Kohlstedt (1984, 1986); Takei & Holtzman (2009a)) and Nabarro-Herring creep (diffusion through the grain volume). Diffusion-creep models predict a more rapid decrease in the shear viscosity with porosity than uniform viscous fluid models, but a more modest variation in compaction viscosity. For small porosity, the Nabarro-Herring creep models have a weak (logarithmic) singularity in compaction viscosity, and Coble creep models have a compaction viscosity

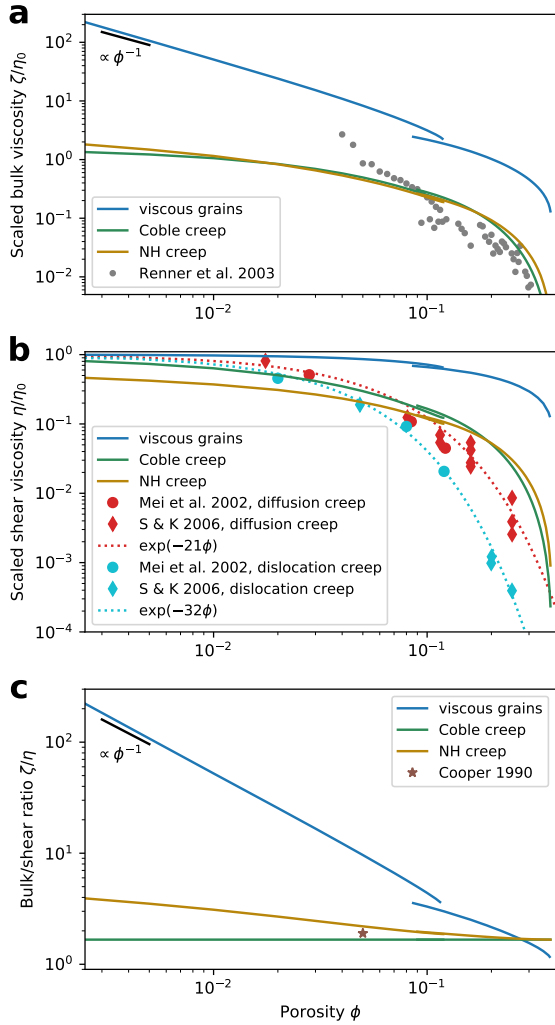


Figure 2

Models and experimental data on the effective viscosities of partially molten rocks as a function of porosity. a) shows the compaction (also known as bulk) viscosity ζ , scaled by η_0 , the shear viscosity in the limit of zero porosity; b) shows the shear viscosity η , also scaled by η_0 ; c) shows the ratio of the compaction viscosity to the shear viscosity. In each panel, three model curves are shown as solid lines. Each model has the same melt geometry, but different grain-scale physics. The geometry assumes textural equilibrium for truncated octahedral grains with a dihedral angle of 40° , as illustrated in **Figure 1**. A break in the curves occurs around 10% porosity due to a topological transition when the square faces become wetted. The curves labelled “viscous grains” assume the matrix of solid grains acts as a uniform viscous fluid, where the interior of each grain is deforming. The other curves are based on grain-scale models of diffusion creep (Rudge (2018b)), where individual grains are rigid and relative motion is accommodated by the plating out or removal of matter at grain boundaries. For compaction viscosity, the C-423 and C-479 (olivine + Li-silicate melt) experimental data of Renner et al. (2003) are shown, scaled assuming $\eta_0 = 2 \times 10^{13}$ Pa s. Different choices of η_0 would move data up and down on the plot, but would not change the relative positions of the data points. For shear viscosity, the compilation of experimental data on dry, synthetic peridotites by Scott & Kohlstedt (2006) is shown, along with the data on olivine + basalt aggregates deformed under hydrous condition by Mei et al. (2002). Dotted lines show the exponential-law fits to the Scott & Kohlstedt (2006) data, $\eta = \eta_0 \exp(-\alpha\phi)$, where $\alpha = 21$ for diffusion creep and $\alpha = 32$ for dislocation creep. Mei et al. (2002) suggest slightly different fit parameters (not shown), with $\alpha = 26$ for diffusion creep and $\alpha = 31$ for dislocation creep. The bulk/shear ratio panel shows a single estimate of the bulk/shear ratio from a four-point bending experiment by Cooper (1990).

that is $5/3$ times the shear viscosity (Takei & Holtzman 2009a; Rudge 2018b).

Laboratory experiments have been performed to estimate the shear viscosity of partially molten rock, but few have attempted to estimate the compaction viscosity (notable exceptions are Cooper (1990) and Renner et al. (2003)). The experimental studies on shear viscosity (e.g., Scott & Kohlstedt (2006); Mei et al. (2002), **Figure 2**) indicate a slightly more rapid drop-off in the shear viscosity with increasing porosity than the diffusion-creep models predict; this may be due to effects not captured by an idealized melt geometry, e.g., anisotropic surface energies that cause wetting of grain boundaries at smaller porosity. It should be noted that the experimental data in **Figure 2** are limited to relatively high porosity ($\phi \gtrsim 1\%$), higher than typical mantle porosity ($\phi \sim 0.1\%$, McKenzie (2000)).

The rheological behaviour of partially molten rock at very small porosity ($0 \leq \phi <$

0.01%) is poorly understood. In this case, additional physical processes need to be taken into account. For example, the models shown in **Figure 2** assume an infinite diffusivity in the melt phase, whereas at sufficiently small porosity, the finite diffusivity of the melt can be the rate-limiting control on the shear viscosity (Takei & Holtzman (2009b)). It has been suggested, both theoretically (Takei & Holtzman 2009a) and experimentally (Faul & Jackson (2007); McCarthy & Takei (2011)), that very small fractions of melt can lead to a drop in the shear viscosity from melt-free values by a factor of 5 or more. The theoretical argument of Takei & Holtzman (2009a) is based on the notion that very small amounts of melt can act as a significant fast path for diffusion. Subsequent calculations have determined a more modest weakening due to this effect (Rudge 2018b). Moreover, recent studies have suggested that much of the weakening seen in experiments might be attributable to sub-solidus phenomena, such as the development of premelting films on grain boundaries as the solidus temperature is approached from below (Yamauchi & Takei 2016; Takei 2017).

A major shortcoming of most existing models of upscaled physical properties such as permeability or viscosity is that they assume a fixed microstructure. When a partially molten rock is deformed, its microstructure can change substantially, and this can have a significant effect on macroscale properties. For example, Takei (2005) observes significant additional wetting of grain boundaries in rock-analogue borneol samples placed under shear, with corresponding changes in their elastic, anelastic, and viscous properties. Moreover, grain size is not a fixed quantity, but evolves in time (e.g., grain growth, Breithaupt et al. (2021)) and with deformation (e.g., dynamic recrystallization, Austin & Evans (2007)). Models that capture the evolution of microstructure during deformation are in their infancy, but there have been some notable developments. In particular, Takei & Holtzman (2009c) show how an anisotropic microstructure leads to an anisotropic effective viscosity for Coble creep. Such an anisotropic viscosity couples shear and bulk deformation, and can explain laboratory experiments on partially molten rocks deformed in torsion that show radial segregation of melt (Qi et al. 2015). Bercovici & Ricard (2012) have introduced a continuum, two-phase flow formalism with evolution equations for average properties of the microstructure, such as grain size and interface curvature, but we do not yet have models that capture a time-evolving anisotropic fabric.

2.3. The compaction length

Viscously-deformable porous media have a natural lengthscale δ , the compaction length, which is defined as (McKenzie 1984)

$$\delta = \sqrt{\frac{k}{\mu} \left(\zeta + \frac{4}{3}\eta \right)}. \quad (2)$$

The compaction length sets the scale over which compaction occurs when there is an obstruction to flow. It controls the thickness of boundary layers and the spacing of localisation features. It depends on the melt viscosity μ , as well as the permeability k , the shear viscosity η , and the compaction viscosity ζ , whose dependence on the grain-scale physics has been discussed in the previous subsections.

While there is still much uncertainty in the appropriate values for the parameters in equation (2), it is possible to make order-of-magnitude estimates for typical compaction lengths in the mantle beneath ridges (Kelemen et al. 1997). Taking a typical shear viscosity $\eta \sim 5 \times 10^{19}$ Pa s, a typical compaction viscosity $\zeta = \frac{5}{3}\eta$, a typical melt viscosity $\mu \sim 10$ Pa s,

a porosity–permeability relation $k = d^2 \phi^2 / 1600$, and a grain size $d = 3$ mm, we have that $\delta \sim 300$ m for a porosity $\phi = 0.1\%$, and $\delta \sim 3$ km for a porosity $\phi = 1\%$. However, if compaction viscosity were significantly greater than shear viscosity, then the estimates of compaction length will be correspondingly larger. For example, at a porosity of $\phi = 0.1\%$, $\zeta = 550\eta$ for the viscous grain models of **Figure 2**, leading to $\delta \sim 4$ km; and for a porosity of $\phi = 1\%$, $\zeta = 51\eta$, and thus $\delta \sim 12$ km.

2.4. Reactive melting and channelization in the laboratory

As magma moves from higher to lower pressure, its shifting equilibrium chemistry drives incongruent melting reactions (Longhi 2002). The pressure variation within the mantle is dominantly vertical, although gradients also occur due to dynamical effects. The decrease in pressure as magma rises leads it to become undersaturated in silica. Silica-undersaturated magma in turn reacts with the mantle rock, dissolving pyroxene and precipitating olivine (harzburgite \rightarrow dunite). This dissolution reaction leads to a net transfer of mass from the rock to the magma phase, and so this process is sometimes called reactive melting (Kelemen 1990). Dunite channels found in ophiolites (**Figure 3c**) are interpreted as the geological remnant of this process (Kelemen et al. 1992; Braun & Kelemen 2002), suggesting that melt flow was focussed in the regions that became the dunites rather than being distributed uniformly.

Laboratory experiments help us to understand the physical and chemical controls that lead to channelized flow. The large-scale solubility gradient driving reaction in the mantle is impossible to realize in the laboratory. Instead, a similar chemical reaction is created by placing a melt reservoir that is undersaturated in silica (an alkali basalt) next to a partially molten rock formed from a mixture of olivine and pyroxene (**Figure 3a**). This creates a sharp jump in undersaturation, in contrast to the gradual gradient in the mantle (**Figure 3d**). Infiltration of melt from the reservoir into the partially molten rock drives the same type of chemical reaction that occurs in the mantle.

However, the mere existence of undersaturation is insufficient to cause reactive channelization. Experiments by Morgan & Liang (2003) without forced melt flow produced reactive dissolution in a fringe between the melt source and the partially molten rock; the thickness was controlled by chemical diffusion. They observed no marked channelization (**Figure 3e**).

Rather, sufficiently rapid melt flow is required for reactive channelization. Pec et al. (2015, 2017) also conducted contact-style experiments at conditions similar to the mantle. They applied a pressure gradient to drive melt from the reservoir into the partially molten rock, without significantly affecting the equilibrium chemistry. If the pressure gradient, and hence the melt velocity, was high enough, the reactive front localized into reactive channels (**Figure 3f**). Pec et al. (2020) extended these experiments by considering a range of types of partially molten rock (werhlite, harzburgite, lherzolite). They showed that the critical conditions for channelization varied with the type of rock. While werhlite and harzburgite samples had tube-shaped channels (**Figure 3b**), lherzolite samples sometimes had vein-shaped channels. The latter was tentatively attributed to a fracture-like phenomenon.

Dunite channels found in ophiolites have a tabular morphology (Kelemen et al. 1992; Braun & Kelemen 2002), which contrasts with the tube-shaped channels found experimentally. More broadly, although the chemistry of the reaction in the experiments is similar to that in the mantle, the fluid dynamical aspects (that are crucial to the instability) are

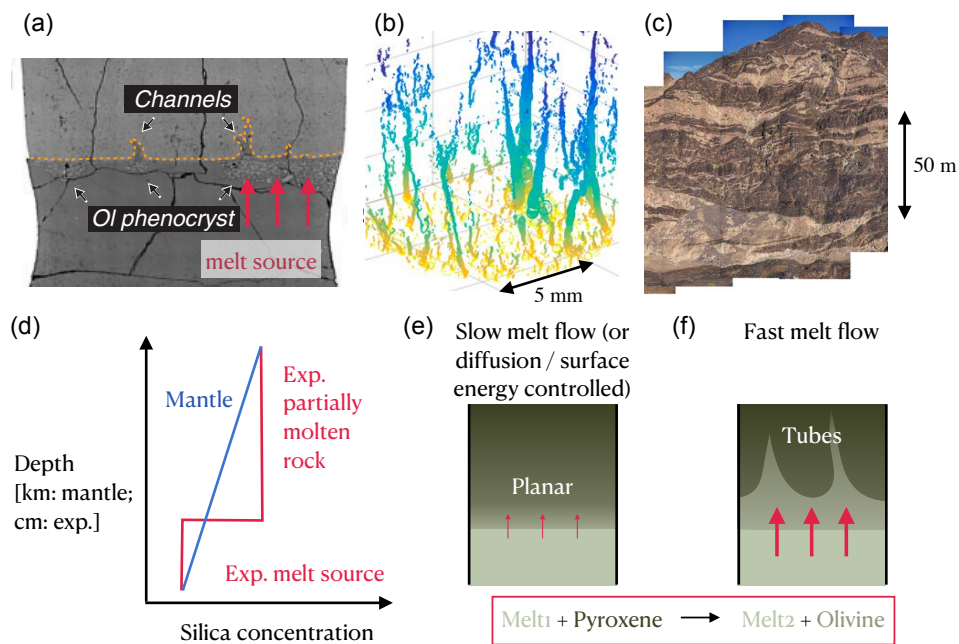


Figure 3

(a) Experiments where melt is driven into a partially molten rock causing channels to form (panel adapted from Pec et al. 2017). (b) CT scan showing that the channels are tube-shaped (panel adapted from Pec et al. 2020). (c) Field observations of tabular dunites from the Muscat Massif ophiolite (panel adapted from Braun & Kelemen 2002). The paleogravity direction is perpendicular to the present exposure such that the dunites would have been near vertical at the time of formation. (d) Schematic diagram of reaction channelization. Silica concentration varies gradually with depth in the mantle and has a stepwise jump in the experiments between an undersaturated melt reservoir and the partially molten rock sample. (e) For slow melt flow, there is a near-planar reaction front. (f) For fast melt flow, tube-shaped reactive channels emerge.

different between the settings. Therefore, modelling has a significant role in interpreting these laboratory experiments in terms of melt extraction from the mantle, a question we turn to in sec. 3.2.1. Moreover, the experiments showed that microphysical properties of the partially molten rock control whether or not channelization occurs. These properties must therefore be characterized both at the laboratory scale and at the tectonic scale.

3. PHYSICS OF MELT EXTRACTION IN THE ASTHENOSPHERE

Asthenospheric melt transport operates on timescales, over pressure gradients and at strain rates that will never be accessible in laboratory experiments. These scales also make the natural setting inaccessible to direct observation; measurement of proxies for the quantities of interest is usually the best we can do. Physics-based models are then required to interpret the proxy data, and this complicates the testing of models against data. Ultimately, however, it is the quantitative consistency between laboratory physics, observations of nature, and theoretical models that gives confidence in a physical understanding of the natural system. In this section we review constraints derived from observations and models

based on our understanding of the physics.

3.1. Observational proxies of magma speed

3.1.1. Uranium series. Important constraints on the speed of melt transport through the mantle come from observations of U-series disequilibria in lavas. The basic premise in using U-series to provide minimum bounds on ascent speeds is simple, but there are many subtleties in practice. Before the mantle melts, it is in a state of radioactive equilibrium where each intermediate isotope in a decay chain is produced at approximately the same rate as it decays. On melting, some elements more readily enter the melt than others, causing the decay chain to be out of equilibrium in the melt. Isotopes in the chain return to radioactive equilibrium on a timescale set by their half-life. If radioactive disequilibrium is seen at the surface, it means that the transport process must have taken place within a few half-lives of the isotope in question.

The subtleties arise in identifying the particular physical process that causes the disequilibria, and identifying the depth at which that process takes place. For example, some isotopes in the decay chains (e.g., ^{210}Pb) have volatile intermediate isotopes, and might be affected by near-surface degassing (Turner et al. 2012). Attributing a near-surface degassing signal to a deep mantle melting signal will lead to a vast overestimate of melt ascent rates. A more robust constraint comes from the observed excesses of ^{230}Th to ^{238}U in mid-ocean ridge basalts. The half-life of ^{230}Th is 75,000 yr. Th is thought to be more incompatible than U only in the presence of garnet. If the source rock is lherzolite, garnet is present only beneath the garnet–spinel transition at ~ 80 km depth. The observed ^{230}Th excesses then constrain the melt ascent rate to be at least 1 m/yr. If the observed excesses in the shorter-lived isotopes ^{231}Pa and ^{226}Ra also originate at such depths, melt transport speeds through the mantle may be 100 m/yr or higher (Stracke et al. 2006; Turner et al. 2001). If the ^{210}Pb disequilibria originate at depth, melt transport would be inferred to be even faster, with transport speeds up to 1 km/yr (Rubin et al. 2005).

Interpretation of U-series is further complicated by the likely lithological heterogeneity of mantle. The presence of garnet pyroxenite allows for garnet signatures of fractionation to be produced at shallower depths (Elkins et al. 2019). For a more detailed discussion of U-series constraints on melt ascent see Elliott & Spiegelman (2003); Turner & Bourdon (2011).

3.1.2. Icelandic eruption chronology. More direct constraints on melt-transport speeds come from observations of the magmatic response to deglaciation in Iceland, particularly during the most recent major deglaciation around 12,000 years ago. Eruption rates surged by a factor of 30 or more following the deglaciation. The most natural explanation for this surge is that unloading of the ice caused mantle rock at depth to rapidly decompress, increasing melting rates, and leading to an increase in eruption rates following the transport of the melt to the surface (Jull & McKenzie 1996). The observed time lag between glacial unloading and the surge in eruption rates yields a bound on the melt transport timescale (MacLennan et al. 2002).

Chemical observations of lavas erupted during and following the periods of deglaciation provide additional information. Notably, lavas erupted during the surge are depleted in Rare Earth Elements (REEs) by up to 70% (MacLennan et al. 2002; Sinton et al. 2005; Eason et al. 2015). Modelling by Eksinichol et al. (2019) has indicated that the chemistry of

the erupted lavas is strongly affected by melt transport speeds, as melts produced at shallow depths are depleted in REEs and are transported to the surface faster than the REE-enriched melts that are produced deeper. Field observations can identify lavas erupted under ice, and the modelling shows the amount of subglacial volcanism is also sensitive to melt transport speeds: more rapid rates of melt ascent lead to a greater fraction of lavas erupting under ice. Eksinchol et al. (2019) concluded that the suite of Icelandic observations are best explained by average rates of melt transport through the mantle of ~ 100 m/yr.

However, rates of melt transport estimated during Iceland's recent deglaciation may not be representative of the rates of melt transport during typical mid-ocean ridge melting. Iceland is underlain by a hot mantle plume that causes a significant increase in melting rates compared with that expected for pure passive upwelling; this is reflected in the thick (~ 20 km) crust beneath much of the island. Furthermore, the melting rates following deglaciation are an order of magnitude greater than the background, steady-state melting rates. Rees Jones & Rudge (2020) used a 1-d melting column model to quantify how unrepresentative the deglaciation estimates are, and conclude that while typical transport rates may be lower than the Icelandic estimates, average melt transport speeds of at least 10 m/yr should be seen across the global ridge system.

BOX A: IMPLICATIONS OF PROXY OBSERVATIONS FOR MELT EXTRACTION

The speed of melt transport, as inferred from the two proxies discussed in sec. 3.1, appears too large to be consistent with the null hypothesis of diffuse porous flow (eqn. (1)). For example, taking 30 m/yr as a characteristic speed at a porosity ϕ of $\sim 0.1\%$, consistency with diffuse porous flow based on the porosity–permeability relation $k = d^2\phi^2/1600$ requires a grain size d of order 5 cm, much larger than observed in mantle xenoliths. An alternative hypothesis is transport through dikes in the solid asthenosphere; this mechanism is observed to occur in the lithosphere (Rivalta et al. 2015). While diking cannot be ruled out on physical grounds, there is no evidence that it occurs in the asthenosphere (except in subduction zones; see sec. 4.2), whereas there is good evidence for porous flow localised into high-flux channels (Kelemen et al. 1997).

Implications of the U-series and deglaciation-volcanism proxies for magma speed are discussed in **BOX A**.

3.2. Mechanisms of flow channelisation

We next review mechanisms of magmatic localisation into channels. We provide some background, but focus on ideas published since this subject was reviewed by Kelemen et al. (1997).

3.2.1. Reactive flow instabilities. Is the reaction infiltration instability a viable mechanism for channelization in the mantle (Aharonov et al. 1995)? To form, channels must grow fast enough compared to the upwelling rate of the mantle. Stability analysis allows us estimate the linear growth rate σ_{react} of channels (Rees Jones & Katz 2018). Three properties control σ_{react} :

1. The potential for reactive melting b [units m^{-1}]. This can be thought of as the ratio

- of the change in the equilibrium concentration of silica in the magma per unit depth divided by the degree of supersaturation of silica in reactive melts.
2. The speed of background melt flow before the onset of channels w_0 [units m yr^{-1}]. Throughout this subsection, we use a subscript $_0$ to denote a steady-state, unchanneled flow.
 3. The sensitivity of permeability to porosity, as expressed by the permeability exponent n [no units].

Extra reactive melting caused by extra melt flow increases the porosity. This positively feeds back on the permeability and hence the melt velocity. Given these properties, a simple first estimate of the maximum growth rate (which we refine below) is

$$\sigma_{\text{react}} = nbw_0. \quad (3)$$

This comes from estimating the extra melt flux per unit extra porosity as nw_0 , which is then multiplied by b to obtain the extra melting. The estimates $n = 2$, $b = 2 \times 10^{-6} \text{ m}^{-1}$, $w_0 = 1 \text{ m yr}^{-1}$ give $\sigma_{\text{react}} = 4 \times 10^{-6} \text{ yr}^{-1}$, or a growth timescale (time in which channel porosity changes by a factor of $e = 2.7$) of $1/\sigma_{\text{react}} = 0.25 \text{ Myr}$. This is significantly less than the upwelling time for a parcel of partially molten mantle to rise across the melting region (about 2 Myr). However, if channels are vertically confined to the shallowest section of the mantle (Rees Jones & Katz 2018), the relevant transit time is shorter. By combining the prediction for the vertical scale of channels from Rees Jones & Katz (2018) with equation (3), channels should form when $n(b\delta)^2 w_0/W_0 \gtrsim O(1)$, where W_0 is the mantle upwelling rate and δ is the compaction length (sec. 2.3). This estimate is consistent with the regime diagram of Hesse et al. (2011), whose linear stability analysis included mantle upwelling, but it needs further investigation in the context of nonlinear modelling. As we have seen, the observational constraints point to faster melt velocity $w_0 > 1 \text{ m/yr}$ (sec. 3.1), at least once melt flow has become channelized.

At what horizontal length scale should we expect channels to emerge? Aharonov et al. (1995) introduced the concept of a reactive length scale L_{eq} , which is the distance travelled at the Darcy velocity before reacting back to chemical equilibrium. Rees Jones & Katz (2018) generalized this concept to include the distance silica diffuses through the melt before reacting back to chemical equilibrium. L_{eq} is highly uncertain, mainly due to the need to extrapolate from laboratory experiments to estimate the reaction rate. A central estimate is $L_{eq} = 10^{-3} \text{ m}$ but this is uncertain within at least a factor of 100 in either direction (Aharonov et al. 1995; Rees Jones & Katz 2018). If the reactions are infinitely fast, then $L_{eq} = 0$, as in equilibrium models (Hewitt 2010).

Compaction affects the linear growth rate of channels in two main ways. The first mechanism occurs even if the compaction viscosity ζ is independent of porosity and depends on the compaction length. If the compaction length $\delta \gtrsim (H/b)^{1/2}$, where H is the depth of the partially molten mantle, then the system is effectively rigid. However, if the compaction length is smaller, then it affects the most unstable wavelength of channels, as discussed by Rees Jones & Katz (2018):

$$\lambda \approx 2\pi \begin{cases} 0.55(L_{eq}H)^{1/2}, & \delta \lesssim (H/b)^{1/2}, \\ \delta(L_{eq}b)^{1/2}, & \delta \gg (H/b)^{1/2}. \end{cases} \quad (4)$$

Estimates indicate λ on the scale of around 1 m, again with significant uncertainty. This

wavelength-dependent compaction has only a minor effect on the growth rate provided $\delta \gg \sqrt{L_{eq}/b} \approx 20$ m, which is expected for the mantle.

The second mechanism relies on the decrease of compaction viscosity with increasing porosity. A linear estimate of the (negative) contribution to the growth rate by this mechanism is

$$\sigma_{\text{compact}} = \frac{-C_0}{\zeta_0 + \frac{4}{3}\eta_0} \left. \frac{d\zeta}{d\phi} \right|_{\phi_0} = \frac{\Gamma_0}{\zeta_0 + \frac{4}{3}\eta_0} \left. \frac{d\zeta}{d\phi} \right|_{\phi_0} \quad (5)$$

where the second equality is based on the steady-state balance between compaction rate and volumetric melting rate $C_0 = -\Gamma_0$, and the slope $d\zeta/d\phi < 0$ (**Figure 2a**). This effect is purely mechanical and is independent of the wavelength of channels. Indeed, if the background state were decompacting ($C_0 > 0$), as would occur in a decompaction channel at the base of the lithosphere, this mechanism would be destabilizing. At the top of the partially molten mantle, we can estimate $\phi_0 w_0 = \Gamma_0 H$. So, by comparing equations (3) and (5), we see that compaction will stabilize the system providing

$$-\frac{\phi_0}{\zeta_0 + \frac{4}{3}\eta_0} \left. \frac{d\zeta}{d\phi} \right|_{\phi_0} > nbH \approx 0.3. \quad (6)$$

A negative contribution to the total growth rate proportional to the slope of $\zeta(\phi)$ was first reported by Hesse et al. (2011). Significant differences between studies arise from choices of $\zeta(\phi)$. Thus, if $\zeta \propto \phi^{-1}$, in which case the left-hand-side of equation (6) is about 1, we should expect compaction to completely stabilize the linear system, as occurred in Hewitt (2010). However, if the sensitivity of $\zeta(\phi)$ is much smaller, the reactive instability can win out, as occurred in Aharonov et al. (1995), which used a constant compaction viscosity (zero slope). Similarly, Hesse et al. (2011) found that compaction–dissolution waves (a generalization of the concept of a reactive channel in which the growth rate has an imaginary part, leading to wave-like behaviour) would be expected in mantle conditions for weak sensitivity but not for strong sensitivity. The diffusion-creep models shown in **Figure 2a** have an intermediate sensitivity. Evidently, understanding rheological properties is crucial.

The significance of compaction stabilization estimated by eqn. (5) does not appear in this general form in the published literature. For the interested reader, we outline a physical derivation that generalizes a discussion by Hewitt (2010) and is similar in spirit to the estimates of the growth rate of shear-driven melt bands by Stevenson (1989). In the absence of macroscopic shear flow, a liquid pressure gradient and buoyancy forcing, momentum conservation requires that $(\zeta + \frac{4}{3}\eta)\nabla\mathcal{C} + \mathcal{C}\nabla\zeta = 0$ (see eqn. (21) in Rees Jones et al. 2021). Thus a gradient in ζ across a channel drives a gradient in compaction rate that tends to reduce porosity in the channel. The linear change in compaction rate $\hat{\mathcal{C}}$ can be related to the change in porosity $\hat{\phi}$ by $(\zeta_0 + \frac{4}{3}\eta_0)\hat{\mathcal{C}} = -\left. \frac{d\zeta}{d\phi} \right|_{\phi_0} C_0 \hat{\phi}$. Finally, mass conservation in the absence of reaction, $\sigma\hat{\phi} = \hat{\mathcal{C}}$, gives the growth-rate estimate (5).

Linear analysis only applies to the initial development of channels. What happens when channels grow beyond the linear regime?

Two-dimensional numerical simulations by Spiegelman et al. (2001) suggest a channel spacing consistent with the predictions of the linear theory. Theoretically, dynamic pressure gradients that in turn drive dynamic solubility gradients could promote the coalescence of channels. However, Rees Jones et al. (2021) argued that such pressure gradients at MORs are typically much smaller than the vertical lithostatic pressure gradient.

The width of the channels, once they develop, is considerably smaller than the spacing and appears to be dominantly controlled by diffusion within the parameter regime explored

Compaction rate \mathcal{C} :

divergence of the solid velocity. \mathcal{C} is negative for a medium that is compacting.

Sensitivity of bulk

viscosity: slope of the compaction viscosity relationship $\zeta(\phi)$, characterised by the dimensionless quantity

$$m = - \left. \frac{d\zeta}{d\phi} \right|_{\phi_0} \frac{\phi_0}{\zeta_0}.$$

This generalizes the exponent in the scaling $\zeta \propto \phi^{-m}$.

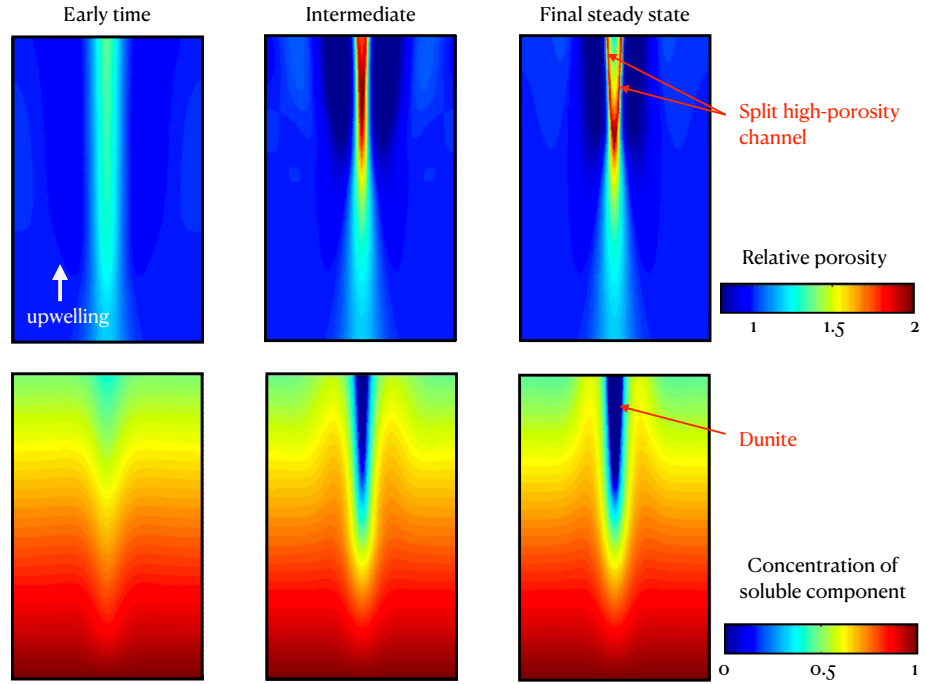


Figure 4

Nonlinear evolution of reactive channels. Upper row shows the relative porosity. Lower row shows the concentration of the soluble component, which is progressively exhausted within the central channel. Figure adapted from Supplementary Movie of Schiemenz et al. (2011) by permission of the authors. See also Liang et al. (2010).

by Spiegelman et al. (2001). As discussed above, the effective diffusive length scale approaches zero as $R \rightarrow \infty$, so calculations based on chemical equilibrium localize to the grid scale (Hewitt 2010). The total flux of melt is dominated by the flow through channels, so arguably the inferences about melt velocity discussed previously should be interpreted as relating to melt velocity in the channels.

Liang et al. (2010) and Schiemenz et al. (2011) performed high-resolution numerical calculations with boundary conditions that favoured the formation of a single channel and explored lithological features of channel formation. **Figure 4** shows an example of the nonlinear evolution of a reactive channel. As the soluble component of the mantle is exhausted within the centre of the channel, the high-porosity region splits into two, with flow focussed on the margins of the dunite. If this picture is correct, it challenges the idea that the dunites themselves are the pathways of channelized flow, which has important geochemical consequences (Liang et al. 2010). Strong compaction occurs in the centre of the channel in these calculations, which were performed with strong compaction-viscosity sensitivity $\zeta \propto \phi^{-1}$; this behaviour is likely to depend on the sensitivity. It is possible that an increase in grain size within the channel, as suggested by experiments (Morgan & Liang 2005), might counteract this tendency, although this idea remains largely unexplored.

A further way that mantle chemistry might affect reactive channelization is the presence of volatile species. Keller & Katz (2016) and Keller et al. (2017) showed that reactive channelization is enhanced by the presence of volatiles, particularly around the onset-depth of dry melting. This is because this depth-region has both a significant gradient in the equilibrium volatile content in the melt and an increasing-upward melt flux. This idea could be analyzed in greater detail. Volatiles might be especially important in driving deep channelization, which appears to be necessary to match geochemical and geophysical observations (Jull et al. 2002; Liu & Liang 2019)

At a MOR, channels are formed in a more complex environment than a simple upwelling column. The prevalent direction of melt flow will include a component toward the ridge axis (for a review, see Sim et al. 2020), leading to reactive channels that also bend toward the ridge axis (Keller et al. 2017). However, the mantle shear flow driven by plate spreading has a rotational component. This acts to rotate channels that form near-vertically such that they tend to point away from the ridge axis (Baltzell et al. 2015; Keller et al. 2017). At the same time, shearing a porosity-weakening material can generate an independent mechanism of melt localization. We discuss this further in sec. 3.2.3.

3.2.2. Lithological heterogeneity. Models based on stability of the linearised governing equations analyse the growth or decay of infinitesimal perturbations to a steady, background state. It is well established, however, that the mantle is heterogeneous in lithology, major-element chemistry, and hence fusibility at a broad range of scales. In this context, it is unclear whether a steady, background state can be defined. If it can, the heterogeneity must be regarded as a finite perturbation to that state. Does this finite perturbation introduce a propensity for channelisation (Lundstrom et al. 2000), and does that propensity overcome stabilising factors such as a porosity dependence of compaction viscosity? The relationship between heterogeneity and channelisation depends on the coupling between thermochemistry and dynamics under melt segregation.

This coupling remains poorly understood. Investigations to date have been heavily weighted to one aspect or the other. Petrological perspectives have focused on the chemistry of eclogite- and pyroxenite-derived melts (Pertermann & Hirschmann 2003a,b; Kogiso et al. 2004b; Kogiso & Hirschmann 2006) and their interaction with the ambient peridotite (Kogiso et al. 2004a). At pressures >2 GPa, this interaction depends on the source composition of the pyroxenite in relation to a thermal divide in its melting behaviour. Pyroxenites more Si-rich than the thermal divide (including eclogites) produce quartz-normative melts at an invariant point; these melts crystallise when they infiltrate peridotite. Pyroxenites on the mafic side of the divide produce Si-undersaturated (nepheline-normative) melts; these react with peridotite to give a net increase liquid fraction. Only the latter can immediately trigger a channelisation feedback.

Geodynamical perspectives have largely ignored the subtleties of the petrology associated with mantle heterogeneity to focus on the physics of magmatism. Schiemenz et al. (2011) represented heterogeneity as a persistent, localised, excess melt influx on the isochemical boundary of a canonical reactive-melting model (**Figure 4**). To go beyond this, a model must incorporate some representation of variability in bulk composition. A straightforward approach uses a two-component thermochemical system, representing fertile and refractory end-members in solid solution, where the solidus and liquidus temperatures increase with concentration of the refractory component. **Figure 5** shows snapshots from numerical simulations using this two-component system. Panels (a)–(c) are from a tectonic-

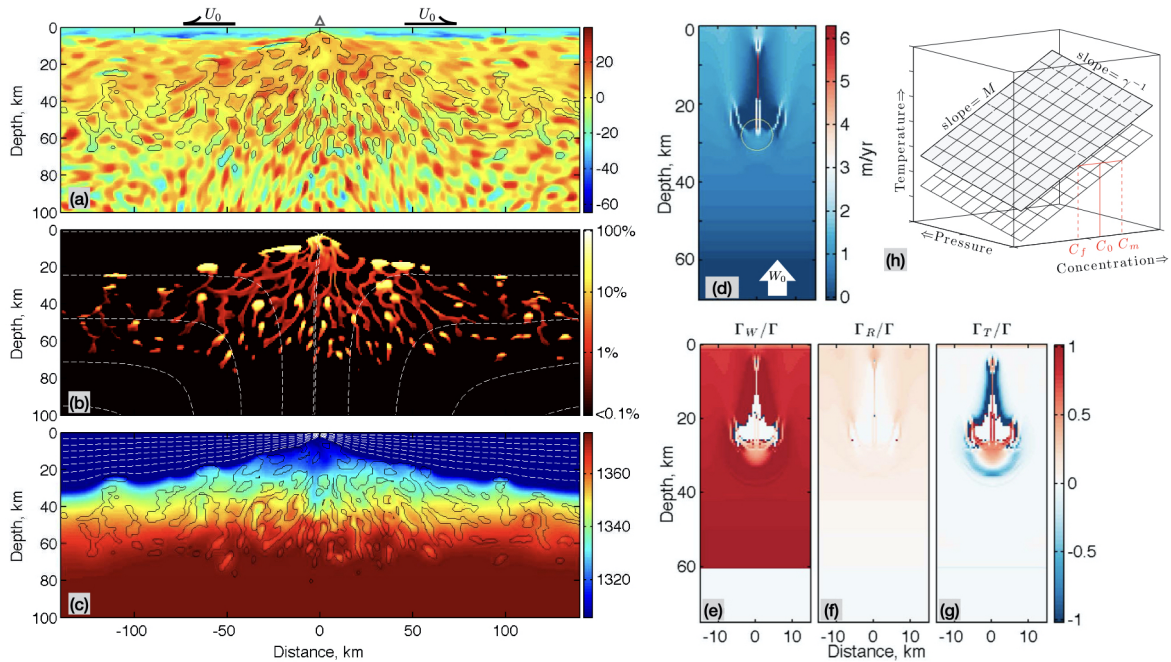


Figure 5

Melting and melt transport in a heterogeneous mantle. Heterogeneity is represented in terms of a two-component, equilibrium thermochemical system with full solid solution. Left-column panels adapted from Katz & Weatherley (2012) show a snapshot from a mid-ocean ridge simulation. Panel (a) shows solidus-temperature differences ($^{\circ}\text{C}$) from a reference value due to chemical heterogeneity. Solid black contour outlines partially molten region. The heterogeneity field, prior to modification by flow or melting, is generated by filtering a random field to remove wavelengths less than 5 km, and rescaling to the desired range of solidus temperature. (b) shows the porosity (%), colours) and streamlines of the solid mantle (white dashed curves). (c) shows potential temperature ($^{\circ}\text{C}$). The colorscale is truncated to highlight temperature variations associated with melting of fertile enclaves, which remain cooler than ambient. The panels at right, adapted from Weatherley & Katz (2012), show a snapshot of a 2-d column with a circular, fertile enclave upwelling at 4 cm/yr. The initial solidus of the enclave is 30°C lower than the ambient mantle at any pressure. Panel (d) shows the magma speed. The white circle outlines where the enclave would be if there were zero melting. Panels (e)–(g) show contributions to the melting rate arising from solid decompression, reactive flow, and thermal diffusion, respectively, as fractions of the total melting rate (see eqn. (7) and text following). Panel (h) shows the linearised phase diagram used to represent petrology in the MOR and upwelling column models. A constant compositional difference ΔC separates the solidus and liquidus surfaces, which have constant slopes M and γ^{-1} in refractory concentration and pressure, respectively.

scale model of a MOR with distributed heterogeneity (Katz & Weatherley 2012), whereas (d)–(g) show an upwelling column with an isolated, initially circular, fertile enclave (Weatherley & Katz 2012). Melting preferentially occurs in fertile regions, both in the more-fusible heterogeneities and the channels that transport their melt. Equilibrium according to the phase diagram fixes their temperature lower than the surrounding refractory regions. Heat from those surroundings diffuses inward, further enhancing melting while suppressing it in the refractory regions (Katz & Rudge 2011). This leads to a key difference from canonical models of reactive flow (sec. 3.2.1), that in the mantle adjacent to channels the porosity is (or approaches) zero. The high-permeability channel is thus contained within a low-permeability jacket. **Figure 5d** shows that melt speed in the channels is enhanced relative

to diffuse porous flow.

Weatherley & Katz (2012) quantify the coupling between (two-component) petrology, thermodynamics and flow. They do so in the context of a linearised phase diagram, as in **Figure 5h**, with solidus temperature that increases with refractory concentration at slope M and a constant difference ΔC in solid–liquid composition. In this case, the volumetric melting rate can be decomposed as

$$\Gamma = \Gamma_W + \Gamma_R + \Gamma_T, \quad (7)$$

where Γ_W represents decompression melting and Γ_R represents reactive melting. The final term, $\Gamma_T = \mathcal{G}\kappa\nabla^2 T \approx \mathcal{G}\kappa M\nabla^2 C_\ell$, represents melting driven by thermal diffusion (chemical diffusion is negligibly slow). Symbol κ represents thermal diffusivity. The contribution from each of these terms is shown as a fraction of Γ in **Figure 5e–g**. The symbol C_ℓ denotes the refractory-component concentration in the liquid, which is related to equilibrium temperature via the phase diagram. Hence a vertical channel carrying fertile melt will have $\Gamma_T \propto \partial^2 C_\ell / \partial x^2 > 0$. A comparison of the contributions of Γ_R and Γ_T indicates that, for the case of a heterogeneity with a significant solidus difference from the ambient mantle, the melting powered by thermal diffusion plays a larger role than that by chemical reaction.

Jordan & Hesse (2015) showed that two-component, solid-solution petrology can also capture the case of melts from a heterogeneity that reactively crystallises to create an impermeable shell. As discussed above, this behaviour is expected for quartz-normative pyroxenite enclaves. Lundstrom et al. (2000) argued that the products of this reactive crystallisation would, at lower pressure, be preferentially melted and drive channelisation. It remains unclear, however, if/how the behaviour predicted in the context of highly simplified petrology (Katz & Weatherley 2012; Weatherley & Katz 2012; Jordan & Hesse 2015; Keller & Katz 2016) is consistent with more realistic petrological models and, indeed, with the natural system.

Melt-transport models of mid-ocean ridges have also illustrated how segregation can create heterogeneity. In simulations by Keller et al. (2017), melt produced in the wings of the melting region ascends to, pools at, and ultimately solidifies into the base of the lithosphere. This metasomatism creates chemical heterogeneity in the lithosphere (Pilet et al. 2008; Rochat et al. 2017). If the melt that crystallises at the lithosphere–asthenosphere boundary is itself derived from a heterogeneous mantle, a recursive petrological process could lead to extreme chemical variability. Alternatively, the dominant pattern of heterogeneity may be simple enough to approximate using a combination of lherzolite, harzburgite, and pyroxenite, in which case inversion methods may constrain their proportions (e.g., Ito & Mahoney 2005; Shorttle et al. 2014). But refractory lithologies, by definition, contribute little to melt production and are therefore difficult to detect (Stracke 2021). Moreover, melt extraction can both create (Spiegelman & Kelemen 2003) and destroy (Bo et al. 2018) geochemical variability, making it difficult to disentangle the effects of source and transport.

3.2.3. Shear-driven melt bands. Laboratory experiments in which a partially molten rock is subjected to shear show melt aligned in sheets (bands in cross section, as we refer to them below) where the porosity is higher than average (Holtzman et al. 2003; Kohlstedt & Holtzman 2009). If the melt bands found in laboratory experiments occur beneath MORs, they would have a significant impact on melt migration. Bands give rise to an anisotropic permeability, with melt preferentially flowing towards or away from the ridge axis depending on their orientation. Katz et al. (2006) showed that a strongly strain-

Prefactor \mathcal{G} :

Thermal cost of melting, units K^{-1} .

$$\mathcal{G} = \frac{1}{L/c_P + M\Delta C}.$$

L is latent heat; c_P is specific heat capacity.

rate-weakening and porosity-weakening shear viscosity gives rise to bands that have an instantaneous growth rate with an alignment that would focus melt towards the ridge axis, potentially explaining the narrowness of the volcanic zone. Melt bands may have further consequences for interpreting geophysical data but here our focus is on melt migration.

Do melt bands grow fast enough in the mantle to matter? And even if they do grow, is this growth robust to other physical mechanisms that might alter or destroy them? What alignment is preferred and how sensitive is this to the degree of strain-rate-weakening, which is generally considered smaller than assumed in Katz et al. (2006). How do melt bands interact with reactive channels and, if both form, which are more important?

A series of studies have addressed these questions. For a sense of how fast melt bands grow, we first discuss their linear growth rate σ_{shear} . Three properties control σ_{shear} :

1. The solid strain rate $\dot{\gamma}_0$ [units s^{-1}].
2. The sensitivity of shear viscosity to porosity.
3. The bulk-to-shear viscosity ratio in the background state.

Given these properties, a simple first estimate of the maximum growth rate, which occurs when extension is orientated across bands, is

$$\sigma_{\text{shear}} = - \left. \frac{d\eta}{d\phi} \right|_{\phi_0} \frac{2\dot{\gamma}_0}{\zeta_0 + \frac{4}{3}\eta_0}. \quad (8)$$

This linear estimate based on a Newtonian rheology from Stevenson (1989) comes from balancing the shear stress associated with viscosity variation across bands with compaction stress. Growth is somewhat faster for a strain-rate-weakening (Katz et al. 2006; Butler 2009) or anisotropic viscosity (Takei & Katz 2015), but (8) is still a good rough estimate, albeit with a different dependence on the angle of porosity bands. Takei & Holtzman (2009c) and Butler (2012) showed that anisotropic diffusion-creep viscosity leads to low-angled bands. Two-phase damage may also be viable mechanism for this (Rudge & Bercovici 2015; Butler 2017). In all models, pressure variation means that growth is suppressed at wavelengths comparable to or greater than the compaction length. See Rees Jones et al. (2021) for further details.

Buoyancy-driven flow is negligible in the laboratory but significant in the mantle. Butler (2009) and Butler (2012) showed that buoyancy-driven flow does not significantly alter the growth of bands but can affect the direction of melt flow.

A further complication is that MOR spreading does not drive a pure-shear mantle flow. Rather, the mantle flow consists of both a shearing part (that drives band formation) and a rotational part (that rotates the bands as they form). This is potentially significant, because bands can be rotated away from orientations in which they grow, to those in which they decay—so analyses based on the instantaneous growth rate like Katz et al. (2006) are probably not a reliable guide to the preferred alignment of bands. Gebhardt & Butler (2016) extended the methodology of Spiegelman (2003) to account for advection and rotation of a small-scale parcel of porosity bands by the mantle corner-flow. The idea is to express the porosity as the sum of a background state ϕ_0 (which varies gradually over the depth of the melting region) and a set of porosity bands with wavenumber $\mathbf{k}(t)$ and log-amplitude $s(t)$: $\phi = \phi_0 + \exp[i\mathbf{k}(t) \cdot \mathbf{x} + s(t)]$. The wavevector and amplitude evolve along streamlines of the solid flow accounting for advection, rotation and growth in amplitude, as shown in **Figure 6a**. They showed that bands which initially point toward the ridge axis are rotated such that they instead focus melt toward the base of the lithosphere.

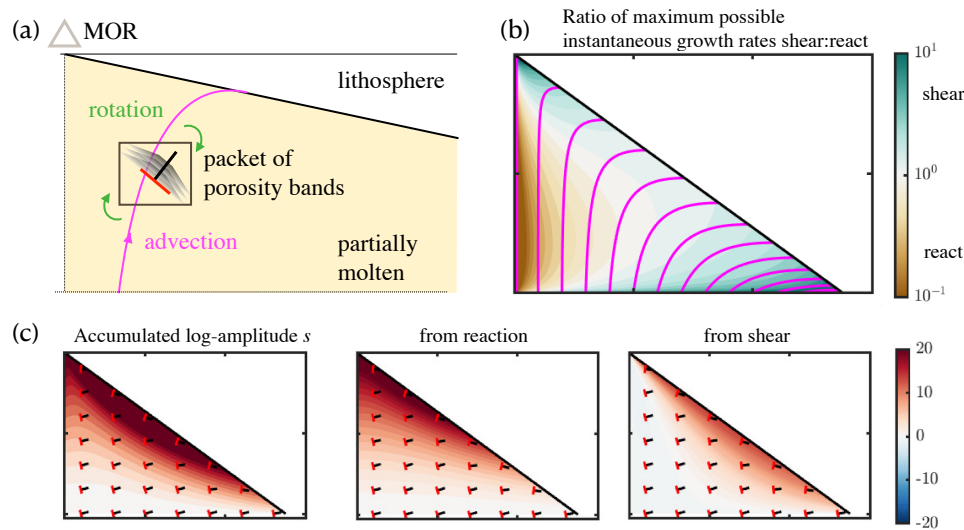


Figure 6

Melt channel and band emergence in a MOR corner flow. **(a)** Sketch of MOR with packet of melt bands that evolves along streamlines of solid flow. **(b)** Ratio of the maximum possible instantaneous growth rates of shear-driven to reaction-driven melt bands. In practice, shear-driven bands are typically orientated such that the actual growth rate is smaller than the maximum. **(c)** log-amplitude of porosity bands where the total is split into reactive and shear contributions. Black line segments show the orientation of the wavevector \parallel and red line segments show the corresponding porosity bands, which are perpendicular to the wavevector, as marked on panel a. Adapted from Rees Jones et al. (2021), CC BY 4.0.

However, reactive channels typically form with a near-vertical alignment, so what happens when both reactive channels and melt bands can form? Rees Jones et al. (2021) accounted for both shear and reactive driven growth. Shear also affects the growth of reactive channels, particularly through the preferred morphology of channels. The ratio of instantaneous shear to reactive growth is controlled by the ratio $\sigma_{\text{shear}}/\sigma_{\text{react}}$, plotted in **Figure 6b**. In the absence of shear, reactive channels form with cylindrical shape. Embedded in an extensional shear flow, reactive channels form as tabular bodies, the orientation of which is vertical when $\sigma_{\text{react}} \gg \sigma_{\text{shear}}$ and controlled by shear when $\sigma_{\text{shear}} \gg \sigma_{\text{react}}$. Rees Jones et al. (2021) showed that reaction dominates shear over most of the MOR system, except near the base of the lithosphere (**Figure 6c**). Channels form deep within the mantle, favouring a subvertical orientation that is then rotated away from the ridge axis. Thus reactive infiltration in the presence of shear is an important mechanism of deep channelization that explains the observed tabular dunites and the disequilibrium between erupted lavas and the upper mantle. Shear may also affect melt migration near the base of the lithosphere, but it probably does not contribute to focusing melt towards the ridge axis.

3.2.4. Decompaction weakening and failure. Could channelised melt flow occur by a purely mechanical process? Connolly & Podladchikov (1998, 2007) proposed a rheological model that incorporates material yielding in response to liquid overpressure. By including this into the canonical theory for partially molten rocks, they showed how it causes magmatic

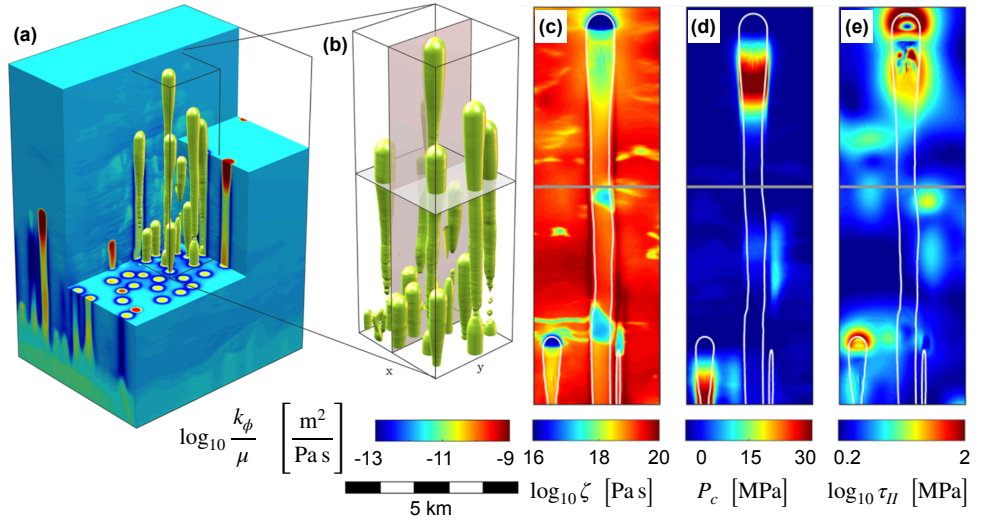


Figure 7

High-resolution 3-D model of buoyancy-driven segregation with decompaction yielding presents gravity-aligned, melt-rich channels. Results rescaled from Räss et al. (2018) to properties of partial melt in the mantle ($\phi_0 = 0.01$, $\zeta_0 = 10^{20}$ Pa s, $k_{\phi_0}/\mu_0 = 1.25 \times 10^{-14}$ m²/(Pa s), $\delta_0 = 1.12$ km). (a) Colors show Darcy coefficient k/μ with warm colours indicating localisation in melt content and hence melt speed. Inset (b) shows isosurfaces of k/μ outlining channel geometry. Vertical cross-sections taken along the grey plane in (b) show compaction viscosity, ζ , in (c) is weakened where compaction pressure, $P_c = (1 - \phi)(P_s - P_\ell)$, in (d) is negative and shear stress magnitude, τ_{II} , in (e) is elevated. Adapted from Räss et al. (2018), CC BY 4.0.

solitary waves to elongate and become gravity-aligned channels.

The rheological formulation of Connolly & Podladchikov (2007) hypothesises that the compaction viscosity ζ (sec. 2.2) is 10^2 – 10^3 times smaller for decompaction as for compaction. In other words, the compaction viscosity depends on the sign of the pressure difference between liquid and solid, such that opening pores induces less viscous resistance than closing them. This asymmetry is a yield-stress behaviour. Such behaviour is clearly applicable to soils and poorly consolidated sediments, where yielding depends on the effective pressure, which is proportional to the interphase pressure difference. At the high temperatures prevalent in the mantle, however, textural equilibrium is maintained on a timescale of ~ 30 yr (sec. 2). In textural equilibrium, incremental adjustments to interphase pressure differences should be symmetrical with respect to the sign of the difference. The conditions under which decompaction yielding can break textural equilibrium, and hence this symmetry, are unknown and require further research. However, processes that create sufficiently rapid variations in melt pressure could potentially nucleate viscoplastic solitary waves.

Solitary wave solutions are a well-studied feature of poro-viscous magma dynamics. They are isolated forms of porosity variation that propagate with constant speed and shape. At their leading edge, magmatic buoyancy gives a liquid overpressure ($P_\ell > P_s$) that causes decompaction, while at the trailing edge it gives a liquid underpressure ($P_\ell < P_s$) that causes compaction. If the compaction viscosity ζ is independent of the sign of the pressure

difference (as typically assumed) and the background state is uniform, then the porosity wave is symmetrical across a plane through its maximum and normal to gravity. In contrast, when the compaction viscosity is different for compaction (ζ_-) and decompaction (ζ_+), then the tail is longer than the head by a factor of $\sqrt{\zeta_-/\zeta_+}$, the ratio of compaction lengths (sec. 2.3). Connolly & Podladchikov (2007) took a central estimate of 30 for this factor, in which case the resulting waves have the form shown in **Figure 7**: channel-like structures with elevated porosity surrounded by a compacted sheath.

These structures focus porous flow and hence increase its speed. The resulting channels would promote reactive melting and dunite formation in a cylindrical geometry. While this hypothesis for reactive melt extraction has not been investigated, Räss et al. (2019) has applied the theory to sedimentary basins as a hypothesis to explain fluid-escape pipes (Cartwright & Santamarina 2015). The plastic theory has been elaborated by Keller et al. (2013) and Yarushina et al. (2020) and is discussed further in the context of lithospheric magmatism (sec. 4.3).

3.3. Climate cycles, sea level & magmatism

The increase of Icelandic volcanism during the last deglaciation is consistent with the contemporaneous global trend of increased eruption rates of glaciated subaerial volcanoes (Huybers & Langmuir 2009, see also section 3.1.2). Glacial cycles are also cycles of sea-level (SL) variation, and so they may affect the submarine mid-ocean ridge system, which is the volumetrically dominant output of magma from the mantle. Deglaciation increases SL which in turn suppresses MOR magmatism. Huybers & Langmuir (2009) hypothesised that MOR magmatism is modulated by glacial cycles, and this idea was subsequently investigated by Lund & Asimow (2011), Crowley et al. (2014) and Cerpa et al. (2019); our present discussion is based on these three papers with a particular focus on the last one.

The plausibility of a sea-level control on MOR magmatism is indicated by the following scaling argument (Lund & Asimow 2011). Background decompression melting beneath a MOR occurs at a rate proportional to $\rho_s g W_0$, whereas modulations of the melting rate scale with the pressure-rate of sea-level variation $\rho_w g \Delta S / \Delta t$, where ρ_w is the density of water. A typical upwelling rate is $W_0 \sim 3$ cm/yr whereas deglaciation can cause an increase in sea level of $\Delta s \sim 100$ m over $\Delta t \sim 10$ kyr. The ratio of SL perturbations to background decompression rates is thus approximately 10%, a level at which one might expect observable consequences.

To understand this system in more detail, we first consider forcing by a monochromatic, sinusoidal SL variation with period t_{SL} . It is helpful to quantify the magmatic response in terms of the amplitude ratio of ridge-axis magma supply to the SL forcing. This ratio is termed the admittance and is plotted as a function of frequency $1/t_{SL}$ in **Figure 8a**. The melting rate is enhanced in proportion to the rate of decrease of SL, $-\dot{S}$. Therefore, if melt transport were instantaneous, there would be zero lag between this rate and the magma supply fluctuations at the ridge axis. The lag predicted on the basis of monochromatic forcing and finite melt-transport speed is plotted in **Figure 8b** as a function of frequency.

We now explain the behaviour shown in these graphs. The SL-enhanced melting rate affects admittance via two mechanisms: (1) an instantaneous, local change of porosity and hence melt flux; (2) the time-dependent segregation of the additional melt generated. At low frequencies, the admittance increases in proportion to the melting-rate forcing, which scales with SL frequency. In this limit, mechanism (1) is negligible and the extra

Monochromatic SL:

A sinusoidal deviation from the mean, where ΔS is the peak-to-trough amplitude and t_{SL} is the period.

Admittance: Ratio of maximum amplitude of fluctuating melt flux to the mean melt flux per unit SL forcing.

Lag: Time between the peak rate of SL drop ($-\dot{S}$) and the subsequent peak in melt flux.

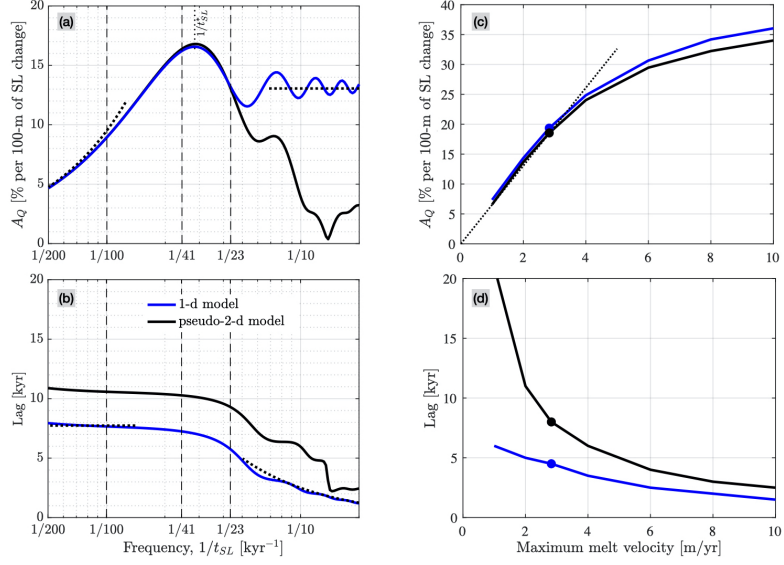


Figure 8

Magmatic response of the (dry) MOR melting region to sea-level variation, adapted from Cerpa et al. (2019), computed with reference parameters of that paper, including $H = 65$ km and $W_0 = 2$ cm/yr. Blue curves show results from the 1-d column model; solid black curves from a pseudo-2-d model that incorporates lateral melt focusing at a finite rate. Vertical dashed lines mark Milankovitch orbital frequencies. Panels (a) and (b) show the response spectrum to a monochromatic, sinusoidal SL forcing using a reference melt speed w_0 of 2.8 m/yr. Compare to fig. 2a of Crowley et al. (2014). Dotted black lines in panel (a) are the solutions at small and large frequencies (eqn. (9)). Panels (c) and (d) show the average response to broadband forcing by reconstructed Pleistocene sea level, as a function of w_0 . Filled circles indicate the value of w_0 used to compute panels (a) and (b). The black, dotted line in panel (c) represents the high-frequency limit in eqn. (9) with $\Delta S = 125$ m. See Cerpa et al. (2019) for further details.

melt segregation is proportional to the forcing by mechanism (2). Hence the melt flux at the top of the column is in phase with $-\dot{S}$. At high frequencies, the admittance tends to a frequency-independent value. In this limit, melt segregation (mechanism (2)) over one period is negligible and the SL amplitude determines the amplitude of the porosity perturbation. The melt flux admittance is a factor n larger than that of porosity due to the permeability–porosity relationship (section 2.1). In this limit, melt flux at the top of the column is in phase with $-\dot{S}$, which peaks a quarter of a period later than its derivative, $-\dot{S}$. These physical considerations lead to the following estimates, which agree well with the numerical calculations in **Figure 8**:

$$A_Q \approx \begin{cases} 2\pi \frac{\rho_w}{\rho_s} \frac{\Delta S}{W_0} \frac{1}{t_{SL}}, & \text{Lag} \approx \begin{cases} \frac{1}{n+1} \frac{H}{w_0}, & t_{SL} \gg t_{SL}^* \text{ (low frequency),} \\ \frac{t_{SL}}{4}, & t_{SL} \lesssim t_{SL}^* \text{ (high frequency),} \end{cases} \end{cases} \quad (9)$$

where t_{SL}^* is the critical sea-level forcing period that gives the maximum admittance.

The maximum admittance is attained when the contribution from the instantaneous change in porosity (mechanism 1) is reinforced by an enhanced flux of melt segregating from below (mechanism 2). In particular, reinforcement occurs when the period t_{SL} is an $O(1)$

multiple of the melt travel time scale H/w_0 , such that the two mechanisms constructively interfere. When $t_{SL} = t_{SL}^*$, the admittance is an $O(1)$ multiple higher than the admittance in the high-frequency limit (Fig. 8a). Quantitative estimates of these multiples are affected by n (Cerpa et al. 2019).

Focusing of melts produced off-axis is necessary to explain the crustal thickness and chemistry of mid-ocean ridges. Pseudo-2-d calculations (black curves in **Figure 8**) show that lateral transport increases the predicted lag at all frequencies. The admittance at high frequency is reduced due to cancellation of perturbations of opposite sign. However, at the lower frequencies relevant for glacial cycles, the admittance is essentially unaffected. Therefore, for monochromatic forcing, the peak admittance scales with w_0/W_0 in both 1-d and pseudo-2-d models.

BOX B: IMPLICATIONS OF MAGMATIC VARIATION WITH GLACIAL CYCLES

Hydrothermal venting, crustal thickness & abyssal-hill topography. Chemical analysis of sediment cores (Lund & Asimow 2011; Lund et al. 2016; Middleton et al. 2016; Costa et al. 2017), seismic profiling of oceanic crust (Boulahanis et al. 2020), and spectral analysis of bathymetric transects (Crowley et al. 2014; Huybers et al. 2016), respectively, provide tentative support for the hypothesis that hydrothermal venting, crustal thickness and abyssal-hill topography, respectively, are affected by SL-driven variations in magma supply. Abyssal hills, however, are predominantly associated with normal faults (Goff 2015; Olive et al. 2015); the existence and nature of a relationship between normal-fault spacing and variations in magma supply at time-scales of glacial cycles remains unclear (Huybers et al. 2016).

Climate feedbacks. Glaciated volcanoes release excess CO_2 during deglaciations, which may create a positive feedback on climate warming (Huybers & Langmuir 2009). Submarine volcanoes would undergo excess degassing with some lag after glaciations (drops in SL, fig. 8), which may create a negative feedback on climate cooling (Huybers & Langmuir 2009; Tolstoy 2015). This has been addressed using simplified, low-dimensional climate models (Huybers et al. 2016; Köhler & Munhoven 2020) but remains somewhat speculative. For MOR carbon to pace glacial cycles, its lag behind $-\dot{S}$ should be greater than about 10 ka, which is unlikely if melt transport is as rapid as expected from observational proxies (sec. 3.1 and fig. 8d).

Panels (c) and (d) of **Figure 8** show the average admittance and lag, respectively, obtained by Cerpa et al. (2019) when forcing the model with a Pleistocene SL reconstruction. The spectrum of reconstructed SL is broad; in calculations with different values of maximum melt speed w_0 , the admittance curve will align differently with this spectrum. At $w_0 \lesssim 4$ m/yr, a significant part of the forcing energy is in the high-frequency regime, where $A_Q \propto w_0$ (eqn. 9). In contrast, for larger w_0 (and hence larger peak-response frequency $1/t_{SL}^*$), an increasing portion of the forcing energy is shifted into the low-frequency regime, where the admittance is diminished. This explains the trends in **Figure 8c**. Faster melt transport speed w_0 has a direct effect on the lag, reducing it as shown in panel (d). Melt transport speeds of ~ 30 m/yr, as inferred in sec. 3.1, should confer larger admittance but smaller lag; implications are discussed in Box B.

4. CURRENT FRONTIERS OF RESEARCH

4.1. Subduction-zone magmatism

Rather less is known about the style of melt extraction in subduction zones than at MORs. Where is melt generated and how is this process related to devolatilization of the slab? What are the pathways of melt migration? Addressing these questions will help us to understand the relative narrowness of the volcanic arc compared to the range of depths of fluid release. Seismic and especially MT imaging have been used to infer a broad zone of partial melting and a lateral component of melt migration. A further question, closely related to magmatism, is the following. What proportion of subducted volatile elements such as carbon are transported to the deep mantle? The global carbon cycle over geological timescales depends crucially on this.

Fluid and melt migration through the mantle wedge in subduction zones is subject to the same physical processes as at MORs: buoyancy-driven porous rise, (de)compaction and attendant pressure gradients, plate-driven mantle flow, melting and, potentially, reactive channelization, particularly that driven by volatiles. The permeability structure of the mantle crucially affects melt migration. Cagnioncle et al. (2007) showed that varying a prescribed grain size, and hence permeability, controls whether melts are dragged down with the mantle atop the slab or rise buoyantly through the mantle wedge. They speculated that melts migrate laterally along a decompaction channel at the base of the lithosphere, as is thought to occur at MORs. Wilson et al. (2014) included the effects of compaction on fluid flow and showed the emergence of a decompaction channel. The behaviour of this kind of model is sensitive to choices of material properties (Cerpa et al. 2017; Cerpa et al. 2019). These models are poro-viscous and so do not account for the brittle processes discussed in sec. 4.2.

Arguably the most important limitations of our current understanding relate to the melting process itself. Melting is driven by the flux of volatiles into the mantle region as well decompression. Volatiles have a major effect on melting and rheology, and therefore it is crucial to accurately account for their migration. Thermal models that only account for the flow of the mantle are widely used for subduction zones. However, such models typically have a thermal structure 200–300 K cooler than that inferred from observations (Kelemen et al. 2003). Rees Jones et al. (2018) performed 2-d numerical simulations with an additional prescribed melt flow, showing that melt flow alters the thermal structure of subduction zones (**Figure 9c**), further evidence of the strongly coupled nature of subduction-zone dynamics. This study also proposed a simple model of volatile-driven melting and used it in pseudo-1-d calculations, showing the evolution of melt fraction and temperature along a pathway that traverses the hot core of the mantle wedge and extends through the lithosphere to the surface. These ideas should be tested in higher dimensional models.

Rawson et al. (2016) hypothesised that some features of chemical variability in arc magmas may evidence volatile-driven reactive channeling in the mantle wedge. Others have argued for diapirism as a central mechanism for melt production (e.g., Marschall & Schumacher 2012; Zhang et al. 2020). However, at this stage there are no published 2-d models that account for the coupling between volatile-driven melting, melt segregation and compaction, and two-phase thermal and chemical transport throughout the mantle wedge. This is a key challenge for future modelling and a place where realistic thermochemistry should be coupled with the dynamics of melt migration.

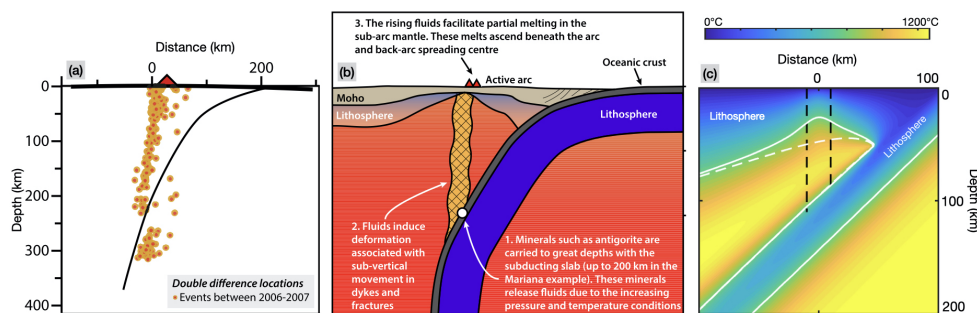


Figure 9

Fluid and thermal transport in subduction zones. **(a)** Earthquake swarm located within the subduction-zone mantle wedge of the Mariana arc, projected from ± 20 km perpendicular to the section (panel adapted from White et al. 2019, CC BY 4.0). **(b)** Schematic diagram explaining the fluid-driven-fracture hypothesis, reproduced from White et al. (2019). **(c)** Subduction-zone thermal structure as modified by fluid transport of heat, after Rees Jones et al. (2018). White contours are 800°C isotherms, with fluid transport (solid) and without (dashed). The imposed Darcian fluid flow is vertical, between the black dashed lines. It has a Gaussian horizontal profile centered at $x = 0$ and a half-width of 10 km. Maximum vertical Darcy flux $\phi w_0 = 3$ m/kyr.

4.2. Ascent through brittle fracture

Is fluid-driven fracture a viable and relevant mechanism for melt transport through the asthenosphere? This was considered plausible but unlikely in the review of Kelemen et al. (1997). The challenge remains in understanding the conditions under which asthenospheric dikes could occur, and whether those conditions prevail anywhere. The key criterion is a liquid pressure that exceeds the minimum compressive stress by the cohesive strength of the rock. To achieve a large and localised liquid overpressure, the timescale of the process creating the overpressure must be short relative to the Maxwell time, which is of order 10 yr in the hot asthenosphere.

Earthquake swarms located within the mantle wedge beneath volcanic arcs provide new evidence that fluid-driven fracture of the asthenosphere is possible (White et al. 2019). **Figure 9a** show carefully relocated hypocentres from a swarm in the Mariana arc, projected onto the diagram from within ± 20 km to the transect. The events form an array connecting the slab to the surface. In this case, no evidence of volcanic activity is found at the surface above the array. In contrast, for a different swarm at the Izu-Bonin arc, the array terminates beneath an active volcano. Centroid moment tensor solutions, computed for the Mariana case only, show double-couple contributions between 10% and 50%. In most cases, the other contribution is from a vertical dipole moment, indicating a net downward acceleration of mass at the source. White et al. (2019) attribute these swarms to high-pressure migration by fluid-driven fracture (**Figure 9b**). They apply a sequence analysis to argue for a melt-transport speed of order 1 km/hr, which is similar to volcanic ascent rates but much faster than indicated by U-series disequilibria or models of channelised flow.

If these interpretations are correct, it raises questions about the relative importance of this mode of transport, the details of the mechanics *in situ*, and the extent to which these mechanics apply in other settings. Sudden fluid release from the cold, brittle slab may create a local overpressure at the base of the wedge and initiate a fracture sequence. But many

Maxwell time: The timescale τ over which a viscoelastic medium relaxes elastic stress by irreversible, viscous flow. $\tau = \eta/E$ where η is the dynamic viscosity and E is the elastic modulus.

questions remain unanswered. Does this process depend on the cool wedge temperatures above the slab and on the low viscosity and low density of the slab-derived fluid? How does the temperature and composition of fluids evolve as they traverse the wedge within fractures? These observations also raise questions with broader relevance. For example, can silicate melts formed during decompression of fertile, volatile-rich, mantle heterogeneities induce fracture? And most importantly, does the absence of recorded seismic swarms in the asthenosphere beneath MORs and hotspot volcanoes imply an absence of fluid-driven fracture there? These questions should motivate further investigation of asthenospheric sources of seismic energy, as well as mechanical models incorporating elasticity and fluid-driven brittle failure (e.g., Keller et al. 2013, and see below).

4.3. Melt at the LAB and in the lithosphere

Melt ascent does not (normally) end at the lithosphere–asthenosphere boundary (LAB), here understood as the thermal boundary where the convection-dominated mantle adiabat steepens into the diffusion-dominated, near-surface geotherm (see review by Rychert et al. 2020). Initially, mantle melt ascending to the LAB will freeze where the temperature sinks below the liquidus of the melt. Crystallisation deposits latent heat and fertile minerals (e.g., pyroxene) into previously cool and refractory mantle lithosphere. This drives the crystallisation front to migrate upwards, moving the LAB with it. If melt supply from the asthenosphere is localised, then this upward migration may establish an undulating permeability boundary (Katz 2008). A decompaction channel beneath this boundary could enhance focussing toward its high points (England & Katz 2010, see also sec. 4.1). Magnetotelluric resistivity imaging has recently produced evidence of possible LAB thermal erosion by melt infiltration near the mid-Atlantic ridge (Wang et al. 2020) and beneath an intraplate volcanic field in northeast China (Li et al. 2021).

At high points of the LAB, melts may accumulate to fractions $>10\%$, well above that of the mantle source region ($<1\%$). They may also differentiate to compositions richer in silica, volatiles and incompatible elements (Jackson et al. 2018). This process had been inferred from geological evidence and described as Melting, Assimilation, Storage, Homogenization (MASH, Hildreth & Moorbath 1988) or as a Deep Crustal Hot Zone (Annen et al. 2006). Toward a more quantitative description, Keller & Suckale (2019) derived a generalised, mixture-theory framework of the transition from low- ϕ porous flow to high- ϕ mushy and suspension flows. The broad interpretation of these magmatic systems is that over time, vertically extensive mush columns develop from which melt-rich magma is extracted to feed volcanic activity (Bachmann & Huber 2019), while the residual crystal-rich mush solidifies into a plutonic rock complex (Cashman et al. 2017). Questions remain, however: What is the spatial extent and distribution of melt-accumulating undulations of the LAB? Does melt reach crustal levels by steady migration of the crystallisation front, or by punctuated, fluid-driven fracture from near the LAB?

Answering the latter question requires an understanding of melt interaction with the rheological transition from ductile asthenosphere to elastic–brittle lithosphere. The Maxwell time (sec. 4.2) increases along the ascent path into cooler rock, which is favorable for fracture. However, melt accumulation at the LAB locally weakens the rock matrix and decreases the Maxwell time, and hence stress may be relaxed before it builds to the point of fracture. Havlin et al. (2013), addressing this problem directly, use a model of dike propagation from the LAB to argue that melt drains into dikes before it accumulates to the point of solid

disaggregation and stress relaxation. Other work has been less focused on specific details of the LAB. Keller et al. (2013), Yarushina et al. (2015) and Yarushina et al. (2020) extend the poro-viscous theory of McKenzie (1984) with a viscoelastic–plastic matrix rheology. Where the cohesive–frictional yield criterion dips to <10 MPa under decompression, the models produce a decompression weakening effect (Connolly & Podladchikov 2007) with an additional dependence on shear stress (Yarushina et al. 2020). At intermediate shear stress, stress-aligned melt-rich bands can emerge, while at higher shear stress, dike-like localisation features become possible (Keller et al. 2013). Further work is needed to understand and validate this rheological formulation in the context of two-phase flow through the lithosphere.

4.4. Coupling petrological thermodynamics

Chemical thermodynamics is central to the physics of magmatism, but has generally been investigated in isolation from the mechanics. The preceding discussion of the relationship between mantle heterogeneity, volatile elements, thermal diffusion, and channelized flow indicates that thermochemistry and mechanics may be tightly coupled. Investigating this coupling with parameterised thermochemistry (e.g., fig. 5) risks missing important interactions between flow, chemical transport and reactions. Transport properties (viscosities, permeability) depend on phase compositions in important and unexplored ways. Moreover, a wealth of existing observations of melts and solid residues could be used to test models that make quantitative petrological predictions.

Incorporating detailed mantle thermochemistry is difficult. It requires tracking at least 10 chemical components in approximately 5 distinct mineral phases, plus the liquid phase. Determining the equilibrium state requires a free-energy minimisation within a large parameter space. The natural system may depart from equilibrium, motivating an additional kinetic theory. Both equilibrium and disequilibrium calculations require empirical thermodynamic data over a vast space of composition, temperature, and pressure. Despite large and growing thermodynamic databases, significant regions of the space remain poorly constrained.

The equilibrium approach has generally involved coupling an existing thermochemical solver for Gibbs-free-energy minimisation with a formulation of multi-phase fluid mechanics. As examples, Tirone & Sessing (2017) uses AlphaMELTS and Oliveira et al. (2020) uses *Perple_X* (see those papers for references to the thermodynamic models). This approach comes with significant computational costs that may be partially mitigated by dynamic optimizations. Other work has focused on development of a theoretical framework for disequilibrium phase change (Šrámek et al. 2007; Rudge et al. 2011), based on irreversible thermodynamics. This has been adapted and used in parameterised thermochemical models (e.g., Keller & Katz 2016; Keller et al. 2017). However, the disequilibrium approach requires calculation of the equilibrium state; with the full set of mantle components, this carries the same costs as for equilibrium thermochemistry. The ENKI project (<http://enki-portal.org>) aims to provide a platform for rigorous thermochemistry that is computationally efficient, open source, and flexible in the choice of thermochemical components. It has been used to model the opx–olivine peritectic and incorporated into model of magmatic segregation that predicts the formation of channels and dunite bodies (Tweed 2021).

Inclusion of full mantle thermochemistry into models of magma segregation promises to expose natural feedbacks on the fluid mechanics and to make predictions that are testable

against petrological observations. In practise, however, this is far from straightforward: inaccuracies in thermodynamic calculations can lead to physical artefacts; computational costs may require problematic sacrifices elsewhere (e.g., grid resolution, parameter space); initial and boundary conditions become more complex; model outputs may be difficult to understand in simple terms (and hence validate). Therefore, while detailed thermochemistry is a frontier of research in the physics of melt extraction, it will not supplant simpler, reduced models anytime soon.

SUMMARY POINTS

1. Observational proxies for the speed of buoyancy-driven melt extraction from upwelling asthenosphere indicate that it is ~ 30 m/yr, faster than can be explained by diffuse porous flow.
2. These observations are consistent with a style of flow in which melt flux is concentrated into high-permeability channels. The channels arise by a reactive flow instability. Mantle heterogeneity, thermal diffusion, and decompaction weakening may reinforce this instability.
3. Quantitative details of the reactive instability depend on material properties, the most important of which are permeability, compaction viscosity, and the chemical thermodynamics of melting and reaction.
4. Pressure variations associated with sea level may drive a $\gtrsim 10\%$ variation in submarine melt extraction, with a lag of ~ 1 ka between forcing and response. If so, this has potentially observable implications.
5. Melt formation, reactive flow, and extraction at subduction zones is a challenging problem due to the petrological and dynamic complexity. Observations of seismic swarms traversing the mantle wedge are probable evidence for fluid-driven fracture as a mode of transport.
6. Coupling melt transport to realistic petrological thermodynamics will improve our understanding of reactive melting and melt extraction. Coupling melt transport to low-temperature rheological models will improve our understanding of melt extraction through the lithosphere, and the mechanical role of magma at plate boundaries.

OUTSTANDING QUESTIONS

1. How are melt geometry, grain-size evolution and rheological properties affected by deviatoric stress and polymineralogy of mantle rocks?
2. What is the relationship between magmatic segregation and reactive channelisation in the context of the fully detailed chemical thermodynamics of the asthenosphere, including volatiles?
3. What is the relationship between mantle heterogeneity, melt production, and melt segregation and what are the observable consequences of this?
4. What is the role, if any, of fluid-driven fracture, decompaction weakening or yielding in asthenospheric melt transport?
5. What is the distribution of melting and melt transport in subduction zones, and how does this feed back on thermal structure, arc position, volatile recycling, and the chemistry of arc magmatism?

6. How does magma interact with the LAB, and how does it traverse the lithosphere, especially in the context of continental and oceanic rifting?

DISCLOSURE STATEMENT

The authors are not aware of any affiliations, memberships, funding, or financial holdings that might be perceived as affecting the objectivity of this review.

ACKNOWLEDGMENTS

The authors acknowledge helpful discussions with O. Shorttle, M. Spiegelman, A. Stracke, and L. Tweed. This research received funding from the European Research Council under Horizon 2020 research and innovation program grant agreement number 772255. The authors thank the Isaac Newton Institute for Mathematical Sciences for its hospitality during the programme Melt in the Mantle which was supported by EPSRC Grant Number EP/K032208/1.

LITERATURE CITED

- Aharonov E, Whitehead JA, Kelemen PB, Spiegelman M. 1995. Channeling instability of upwelling melt in the mantle. *Journal of Geophysical Research: Solid Earth* 100:20433–20450
- Annen C, Blundy J, Sparks R. 2006. The genesis of intermediate and silicic magmas in deep crustal hot zones. *Journal of Petrology* 47:505–539
- Austin NJ, Evans B. 2007. Paleowattmeters: A scaling relation for dynamically recrystallized grain size. *Geology* 35:343–346
- Bachmann O, Huber C. 2019. The inner workings of crustal distillation columns; the physical mechanisms and rates controlling phase separation in silicic magma reservoirs. *Journal of Petrology* 60:3–18
- Baltzell C, Parmentier EM, Liang Y, Tirupathi S. 2015. A high-order numerical study of reactive dissolution in an upwelling heterogeneous mantle: 2. effect of shear deformation. *Geochemistry, Geophysics, Geosystems* 16:3855–3869
- Bercovici D, Ricard Y. 2012. Mechanisms for the generation of plate tectonics by two-phase grain-damage and pinning. *Physics of the Earth and Planetary Interiors* 202–203:27–55
- Bercovici D, Ricard Y, Schubert G. 2001. A two-phase model for compaction and damage 1. General theory. *J. Geophys. Res.* 106
- Bo T, Katz RF, Shorttle O, Rudge JF. 2018. The melting column as a filter of mantle trace-element heterogeneity. *Geochemistry, Geophysics, Geosystems* 19:4694–4721
- Boulahanis B, Carbotte SM, Huybers PJ, Nedimović MR, Aghaei O, et al. 2020. Do sea level variations influence mid-ocean ridge magma supply? A test using crustal thickness and bathymetry data from the East Pacific Rise. *Earth and Planetary Science Letters* 535:116121
- Braun MG, Kelemen PB. 2002. Dunite distribution in the Oman ophiolite: Implications for melt flux through porous dunite conduits. *Geochem. Geophys. Geosys.* 3:8603
- Breithaupt T, Hansen LN, Toppaladoddi S, Katz RF. 2021. The role of grain-environment heterogeneity in normal grain growth: A stochastic approach. *Acta Materialia* 209:116699
- Butler S. 2012. Numerical models of shear-induced melt band formation with anisotropic matrix viscosity. *Physics of the Earth and Planetary Interiors* 200:28–36

- Butler S. 2017. Shear-induced porosity bands in a compacting porous medium with damage rheology. *Physics of the Earth and Planetary Interiors* 264:7–17
- Butler SL. 2009. The effects of buoyancy on shear-induced melt bands in a compacting porous medium. *Phys. Earth Planet. In.* 173:51–59
- Cagnioncle AM, Parmentier E, Elkins-Tanton L. 2007. Effect of solid flow above a subducting slab on water distribution and melting at convergent plate boundaries. *J. Geophys. Res.* 112
- Cartwright J, Santamarina C. 2015. Seismic characteristics of fluid escape pipes in sedimentary basins: implications for pipe genesis. *Marine and Petroleum Geology* 65:126–140
- Cashman KV, Sparks RSJ, Blundy JD. 2017. Vertically extensive and unstable magmatic systems: a unified view of igneous processes. *Science* 355
- Cerpa NG, Rees Jones DW, Katz RF. 2019. Consequences of glacial cycles for magmatism and carbon transport at mid-ocean ridges. *Earth Planet. Sci. Lett.* 528
- Cerpa NG, Wada I, Wilson CR. 2017. Fluid migration in the mantle wedge: Influence of mineral grain size and mantle compaction. *Journal Of Geophysical Research-Solid Earth* 122:6247–6268
- Cerpa NG, Wada I, Wilson CR. 2019. Effects of fluid influx, fluid viscosity, and fluid density on fluid migration in the mantle wedge and their implications for hydrous melting. *Geosphere* 15:1–23
- Connolly JA, Schmidt MW, Solferino G, Bagdassarov N. 2009. Permeability of asthenospheric mantle and melt extraction rates at mid-ocean ridges. *Nature* 462:209–212
- Connolly JAD, Podladchikov YY. 1998. Compaction-driven fluid flow in viscoelastic rock. *Geodynamica Acta* 11:55–84
- Connolly JAD, Podladchikov YY. 2007. Decompaction weakening and channeling instability in ductile porous media: Implications for asthenospheric melt segregation. *Journal Of Geophysical Research* 112:B10205
- Cooper RF. 1990. Differential stress-induced melt migration: An experimental approach. *J. Geophys. Res.* 95:6979
- Cooper RF, Kohlstedt DL. 1984. Solution-precipitation enhanced diffusional creep of partially molten olivine-basalt aggregates during hot-pressing. *Tectonophysics* 107:207–233
- Cooper RF, Kohlstedt DL. 1986. Rheology and structure of olivine-basalt partial melts. *J. Geophys. Res.* 91:9315
- Costa KM, McManus JF, Middleton JL, Langmuir CH, Huybers P, et al. 2017. Hydrothermal deposition on the Juan de Fuca Ridge over multiple glacial–interglacial cycles. *Earth And Planetary Science Letters* 479:120 – 132
- Crowley JW, Katz RF, Huybers P, Langmuir CH, Park SH. 2014. Glacial cycles drive variations in the production of oceanic crust. *Science* 347:1237–1240
- Eason DE, Sinton JM, Grönvold K, Kurz MD. 2015. Effects of deglaciation on the petrology and eruptive history of the Western Volcanic Zone, Iceland. *Bull. Volcanol.* 77:47
- Eksinhol I, Rudge JF, MacLennan J. 2019. Rate of melt ascent beneath iceland from the magmatic response to deglaciation. *Geochemistry, Geophysics, Geosystems* 20:2585–2605
- Elkins LJ, Bourdon B, Lambart S. 2019. Testing pyroxenite versus peridotite sources for marine basalts using u-series isotopes. *Lithos* 332:226–244
- Elliott T, Spiegelman MW. 2003. Melt Migration in Oceanic Crustal Production: A U-series Perspective. In *Treatise on Geochemistry*, eds. KK Turekian, HD Holland. Elsevier, 465–510
- England PC, Katz RF. 2010. Melting above the anhydrous solidus controls the location of volcanic arcs. *Nature* 467:700–703
- Faul UH, Jackson I. 2007. Diffusion creep of dry, melt-free olivine. *Journal of Geophysical Research: Solid Earth*) 112
- Fowler AC. 1984. On the transport of moisture in polythermal glaciers. *Geophysical And Astrophysical Fluid Dynamics* 28:99–140
- Gebhardt D, Butler S. 2016. Linear analysis of melt band formation in a mid-ocean ridge corner flow. *Geophysical Research Letters* 43:3700–3707
- Goff JA. 2015. Comment on “Glacial cycles drive variations in the production of oceanic crust”.

- Science* 349:1065–1065
- Havlin C, Parmentier E, Hirth G. 2013. Dike propagation driven by melt accumulation at the lithosphere–asthenosphere boundary. *Earth and Planetary Science Letters* 376:20–28
- Hesse MA, Schiemenz AR, Liang Y, Parmentier EM. 2011. Compaction-dissolution waves in an upwelling mantle column. *Geophys. J. Int.* 187:1057–1075
- Hewitt IJ. 2010. Modelling melting rates in upwelling mantle. *Earth And Planetary Science Letters* 300:264–274
- Hewitt IJ, Fowler AC. 2008. Partial melting in an upwelling mantle column. *Phil. Trans. R. Soc. London A*
- Hildreth W, Moorbath S. 1988. Crustal Contributions to Arc Magmatism in the Andes of Central Chile. *Contributions to Mineralogy and Petrology* 98:455–489
- Holness M, Siklos S. 2000. The rates and extent of textural equilibration in high-temperature fluid-bearing systems. *Chemical Geology* 162:137–153
- Holtzman B, Groebner N, Zimmerman M, Ginsberg S, Kohlstedt D. 2003. Stress-driven melt segregation in partially molten rocks. *Geochem. Geophys. Geosys.* 4
- Huybers P, Langmuir C. 2009. Feedback between deglaciation, volcanism, and atmospheric CO₂. *Earth Plan. Sci. Lett.*
- Huybers P, Langmuir C, Katz RF, Ferguson D, Proistosescu C, Carbotte S. 2016. Comment on “Sensitivity of seafloor bathymetry to climate-driven fluctuations in mid-ocean ridge magma supply”. *Science* 352:1405–1405
- Ito G, Mahoney J. 2005. Flow and melting of a heterogeneous mantle: 1. Method and importance to the geochemistry of ocean island and mid-ocean ridge basalts. *Earth And Planetary Science Letters* 230:29 – 46
- Jackson M, Blundy J, Sparks R. 2018. Chemical differentiation, cold storage and remobilization of magma in the earth’s crust. *Nature* 564:405–409
- Jordan JS, Hesse MA. 2015. Reactive transport in a partially molten system with binary solid solution. *Geochemistry, Geophysics, Geosystems* 16:4153–4177
- Jull M, Kelemen P, Sims K. 2002. Consequences of diffuse and channelled porous melt migration on uranium series disequilibria. *Geochim. Cosmochim. Acta* 66
- Jull M, McKenzie D. 1996. The effect of deglaciation on mantle melting beneath Iceland. *J. Geophys. Res.* 101:21815–21828
- Katz RF. 2008. Magma dynamics with the enthalpy method: Benchmark solutions and magmatic focusing at mid-ocean ridges. *J. Petrology*
- Katz RF. 2021. The dynamics of partially molten rock. Princeton University Press. In press
- Katz RF, Rudge JF. 2011. The energetics of melting fertile heterogeneities within the depleted mantle. *Geochemistry, Geophysics, Geosystems* 12
- Katz RF, Spiegelman M, Holtzman B. 2006. The dynamics of melt and shear localization in partially molten aggregates. *Nature* 442
- Katz RF, Weatherley S. 2012. Consequences of mantle heterogeneity for melt extraction at mid-ocean ridges. *Earth Planet. Sci. Lett.* 335-336:226–237
- Kelemen PB. 1990. Reaction between ultramafic rock and fractionating basaltic magma I. Phase relations, the origin of calc-alkaline magma series, and the formation of discordant dunite. *J. Petrol.* 31:51–98
- Kelemen PB, Dick HJB, Quick JE. 1992. Formation of hartzburgite by pervasive melt rock reaction in the upper mantle. *Nature* 358:635–641
- Kelemen PB, Hirth G, Shimizu N, Spiegelman M, Dick H. 1997. A review of melt migration processes in the adiabatically upwelling mantle beneath oceanic spreading ridges. *Phil. Trans. R. Soc. London A* 355:283–318
- Kelemen PB, Rilling JL, Parmentier EM, Mehl L, Hacker BR. 2003. Thermal structure due to solid-state flow in the mantle wedge beneath arcs. *Geophysical Monograph Series* 138:293–311
- Keller T, Katz RF. 2016. The role of volatiles in reactive melt transport in the asthenosphere. *J.*

Petrol. 57:1073–1108

- Keller T, Katz RF, Hirschmann MM. 2017. Volatiles beneath mid-ocean ridges: Deep melting, channelised transport, focusing, and metasomatism. *Earth And Planetary Science Letters* 464:55–68
- Keller T, May DA, Kaus BJP. 2013. Numerical modelling of magma dynamics coupled to tectonic deformation of lithosphere and crust. *Geophys. J. Int.* 195:1406–1442
- Keller T, Suckale J. 2019. A continuum model of multi-phase reactive transport in igneous systems. *Geophysical Journal International* 219:185–222
- Kogiso T, Hirschmann M, Reiners P. 2004a. Length scales of mantle heterogeneities and their relationship to ocean island basalt geochemistry. *Geochimica Et Cosmochimica Acta* 68:345 – 360
- Kogiso T, Hirschmann MM. 2006. Partial melting experiments of bimineraleclogite and the role of recycled mafic oceanic crust in the genesis of ocean island basalts. *Earth and Planetary Science Letters* 249:188–199
- Kogiso T, Hirschmann MM, Pertermann M. 2004b. High-pressure Partial Melting of Mafic Lithologies in the Mantle. *Journal of Petrology* 45:2407–2422
- Kohlstedt D, Hansen L. 2015. 2.18 - Constitutive Equations, Rheological Behavior, and Viscosity of Rocks. In *Treatise on Geophysics (Second Edition)*, ed. G Schubert. Oxford: Elsevier, 2nd ed., 441–472
- Kohlstedt DL, Holtzman BK. 2009. Shearing Melt Out of the Earth: An Experimentalist’s Perspective on the Influence of Deformation on Melt Extraction. *Ann. Rev. Earth Planet. Sci.* 37:561–593
- Kohlstedt DL, Zimmerman ME. 1996. Rheology of partially molten mantle rocks. *Annual Review of Earth and Planetary Sciences* 24:41–62
- Köhler P, Munhoven G. 2020. Late Pleistocene Carbon Cycle Revisited by Considering Solid Earth Processes. *Paleoceanography and Paleoclimatology* 35
- Li Y, Weng A, Xu W, Zou Z, Tang Y, et al. 2021. Translithospheric magma plumbing system of intraplate volcanoes as revealed by electrical resistivity imaging. *Geology*
- Liang Y, Schiemenz A, Hesse M, Parmentier E, Hesthaven J. 2010. High-porosity channels for melt migration in the mantle: Top is the dunite and bottom is the harzburgite and lherzolite. *Geophys. Res. Letts.*
- Liu B, Liang Y. 2019. Importance of permeability and deep channel network on the distribution of melt, fractionation of REE in abyssal peridotites, and U-series disequilibria in basalts beneath mid-ocean ridges: A numerical study using a 2D double-porosity model. *Earth Planet. Sci. Lett.* 528:115788
- Longhi J. 2002. Some phase equilibrium systematics of lherzolite melting: I. *Geochem. Geophys. Geosys.* 3:1–33
- Lund DC, Asimow PD. 2011. Does sea level influence mid-ocean ridge magmatism on Milankovitch timescales? *Geochemistry Geophysics Geosystems* 12:Q12009
- Lund DC, Asimow PD, Farley KA, Rooney TO, Seeley E, et al. 2016. Enhanced East Pacific Rise hydrothermal activity during the last two glacial terminations. *Science* 351:478–482
- Lundstrom C, Gill J, Williams Q. 2000. A geochemically consistent hypothesis for MORB generation. *Chemical Geology* 162:105–126
- MacLennan J, Jull M, McKenzie D, Slater L, Grönvold K. 2002. The link between volcanism and deglaciation in Iceland. *Geochem. Geophys. Geosys.*
- Marschall HR, Schumacher JC. 2012. Arc magmas sourced from mélange diapirs in subduction zones. *Nature Geoscience* 5:862–867
- McCarthy C, Takei Y. 2011. Anelasticity and viscosity of partially molten rock analogue: Toward seismic detection of small quantities of melt. *Geophysical Research Letters* 38
- McKenzie D. 1984. The generation and compaction of partially molten rock. *J. Petrol.* 25
- McKenzie D. 2000. Constraints on melt generation and transport from u-series activity ratios. *Chemical Geology* 162:81–94

- Mei S, Bai W, Hiraga T, Kohlstedt D. 2002. Influence of melt on the creep behavior of olivine-basalt aggregates under hydrous conditions. *Earth Plan. Sci. Lett.* 201:491–507
- Middleton JL, Langmuir CH, Mukhopadhyay S, McManus JF, Mitrovica JX. 2016. Hydrothermal iron flux variability following rapid sea level changes. *Geophysical Research Letters* 43:3848 – 3856
- Miller KJ, Montési LGJ, Zhu WL. 2015. Estimates of olivine-basaltic melt electrical conductivity using a digital rock physics approach. *Earth Plan. Sci. Lett.* 432:332–341
- Miller KJ, Zhu WL, Montési LGJ, Gaetani GA. 2014. Experimental quantification of permeability of partially molten mantle rock. *Earth Plan. Sci. Lett.* 388:273–282
- Morgan Z, Liang Y. 2003. An experimental and numerical study of the kinetics of harzburgite reactive dissolution with applications to dunite dike formation. *Earth and Planetary Science Letters* 214:59–74
- Morgan Z, Liang Y. 2005. An experimental study of the kinetics of lherzolite reactive dissolution with applications to melt channel formation. *Contributions to Mineralogy and Petrology* 150:369–385
- Olive JA, Behn M, Ito G, Buck W, Escartín J, Howell S. 2015. Sensitivity of seafloor bathymetry to climate-driven fluctuations in mid-ocean ridge magma supply. *Science* 350:310–313
- Oliveira B, Afonso JC, Tilhac R. 2020. A disequilibrium reactive transport model for mantle magmatism. *Journal of Petrology*
- Pec M, Holtzman BK, Zimmerman M, Kohlstedt DL. 2015. Reaction infiltration instabilities in experiments on partially molten mantle rocks. *Geology* 43:575–578
- Pec M, Holtzman BK, Zimmerman ME, Kohlstedt DL. 2017. Reaction Infiltration Instabilities in Mantle Rocks: an Experimental Investigation. *Journal Of Petrology* 58:979–1003
- Pec M, Holtzman BK, Zimmerman ME, Kohlstedt DL. 2020. Influence of lithology on reactive melt flow channelization. *Geochemistry, Geophysics, Geosystems* 21:e2020GC008937
- Pertermann M, Hirschmann M. 2003a. Anhydrous partial melting experiments on MORB-like eclogite: Phase relations, phase compositions and mineral-melt partitioning of major elements at 2–3 GPa. *Journal Of Petrology* 44:2173 – 2201
- Pertermann M, Hirschmann M. 2003b. Partial melting experiments on a MORB-like pyroxenite between 2 and 3 GPa: Constraints on the presence of pyroxenite in basalt source regions from solidus location and melting rate. *Journal Of Geophysical Research-Solid Earth* 108:2125
- Pilet S, Baker MB, Stolper EM. 2008. Metasomatized lithosphere and the origin of alkaline lavas. *Science* 320:916 – 919
- Qi C, Kohlstedt D, Katz R, Takei Y. 2015. An experimental test of the viscous anisotropy hypothesis for partially molten rocks. *Proc. Nat. Acad. Sci.*
- Räss L, Duretz T, Podladchikov YY. 2019. Resolving hydromechanical coupling in two and three dimensions: spontaneous channelling of porous fluids owing to decompaction weakening. *Geophysical Journal International* 218:1591–1616
- Räss L, Simon NS, Podladchikov YY. 2018. Spontaneous formation of fluid escape pipes from subsurface reservoirs. *Scientific reports* 8:1–11
- Rawson H, Keller T, Fontijn K, Pyle DM, Mather TA, et al. 2016. Compositional variability in mafic arc magmas over short spatial and temporal scales: Evidence for the signature of mantle reactive melt channels. *Earth and Planetary Science Letters* 456:66–77
- Rees Jones DW, Katz RF. 2018. Reaction-infiltration instability in a compacting porous medium. *Journal Of Fluid Mechanics* 852:5–36
- Rees Jones DW, Katz RF, Tian M, Rudge JF. 2018. Thermal impact of magmatism in subduction zones. *Earth And Planetary Science Letters* 481:73–79
- Rees Jones DW, Rudge JF. 2020. Fast magma ascent, revised estimates from the deglaciation of iceland. *Earth Plan. Sci. Lett.* 542:116324
- Rees Jones DW, Zhang H, Katz RF. 2021. Magmatic channelization by reactive and shear-driven instabilities at mid-ocean ridges: a combined analysis. *Geophys. J. Int.* 226:582–609

- Renner J, Viskupic K, Hirth G, Evans B. 2003. Melt extraction from partially molten peridotites. *Geochemistry, Geophysics, Geosystems* 4
- Rivalta E, Taisne B, Bungler A, Katz R. 2015. A review of mechanical models of dike propagation: Schools of thought, results and future directions. *Tectonophysics* 638:1–42
- Rochat L, Pilet S, Müntener O, Duret T, Baumgartner L, et al. 2017. Garnet xenocryst from petit-spot lavas as an indicator for off-axis mantle refertilization at intermediate spreading ridges. *Geology* 45:1091 – 1094
- Rubin KH, van der Zander I, Smith MC, Bergmanis EC. 2005. Minimum speed limit for ocean ridge magmatism from ^{210}Pb – ^{226}Ra – ^{230}Th disequilibria. *Nature* 437:534–538
- Rudge JF. 2018a. Textural equilibrium melt geometries around tetrakaidecahedral grains. *Phil. Trans. R. Soc. London A*
- Rudge JF. 2018b. The viscosities of partially molten materials undergoing diffusion creep. *Journal of Geophysical Research: Solid Earth* 123:10–534
- Rudge JF, Bercovici D. 2015. Melt-band instabilities with two-phase damage. *Geophysical Journal International* 201:640–651
- Rudge JF, Bercovici D, Spiegelman M. 2011. Disequilibrium melting of a two phase multicomponent mantle. *Geophys. J. Int.* 184:699–718
- Rychert CA, Harmon N, Constable S, Wang S. 2020. The nature of the lithosphere-asthenosphere boundary. *Journal of Geophysical Research: Solid Earth* 125:e2018JB016463
- Schiemenz A, Liang Y, Parmentier EM. 2011. A high-order numerical study of reactive dissolution in an upwelling heterogeneous mantle—I. Channelization, channel lithology and channel geometry. *Geophys. J. Int.* 186:641–664
- Schmeling H, Kruse JP, Richard G. 2012. Effective shear and bulk viscosity of partially molten rock based on elastic moduli theory of a fluid filled poroelastic medium. *Geophys. J. Int.* 190:1571–1578
- Scott DR, Stevenson DJ. 1986. Magma ascent by porous flow. *J. Geophys. Res.* 91:9283–9296
- Scott T, Kohlstedt D. 2006. The effect of large melt fraction on the deformation behavior of peridotite. *Earth And Planetary Science Letters* 246:177 – 187
- Shorttle O, MacLennan J, Lambart S. 2014. Quantifying lithological variability in the mantle. *Earth and Planetary Science Letters* 395:24–40
- Sim SJ, Spiegelman M, Stegman DR, Wilson C. 2020. The influence of spreading rate and permeability on melt focusing beneath mid-ocean ridges. *Physics of the Earth and Planetary Interiors* :106486
- Simpson G, Spiegelman M, Weinstein M. 2010a. A multiscale model of partial melts: 1. Effective equations. *Journal Of Geophysical Research* 115
- Simpson G, Spiegelman M, Weinstein M. 2010b. A multiscale model of partial melts: 2. Numerical results. *Journal Of Geophysical Research* 115
- Sinton J, Grönvold K, Sæmundsson K. 2005. Postglacial eruptive history of the western volcanic zone, iceland. *Geochemistry, Geophysics, Geosystems* 6
- Sleep NH. 1988. Tapping of melt by veins and dikes. *J. Geophys. Res. Solid Earth* 93:10255–10272
- Spiegelman M. 2003. Linear analysis of melt band formation by simple shear. *Geochemistry, Geophysics, Geosystems* 4
- Spiegelman M, Kelemen P. 2003. Extreme chemical variability as a consequence of channelized melt transport. *Geochem. Geophys. Geosys.* 4
- Spiegelman M, Kelemen P, Aharonov E. 2001. Causes and consequences of flow organization during melt transport: the reaction infiltration instability in compactible media. *J. Geophys. Res.* 106
- Stevenson DJ. 1989. Spontaneous small-scale melt segregation in partial melts undergoing deformation. *Geophysical Research Letters* 16:1067–1070
- Stevenson DJ, Scott DR. 1991. Mechanics of fluid-rock systems. *Annual review of fluid mechanics* 23:305–339
- Stracke A. 2021. A process-oriented approach to mantle geochemistry. *Chemical Geology* 579:120350
- Stracke A, Bourdon B, McKenzie D. 2006. Melt extraction in the Earth’s mantle: Constraints from

- U-Th-Pa-Ra studies in oceanic basalts. *Earth Plan. Sci. Lett.* 244:97–112
- Takei Y. 2005. Deformation-induced grain boundary wetting and its effects on the acoustic and rheological properties of partially molten rock analogue. *Journal of Geophysical Research: Solid Earth* 110
- Takei Y. 2017. Effects of Partial Melting on Seismic Velocity and Attenuation: A New Insight from Experiments. *Ann. Rev. Earth Planet. Sci.* 45:447–470
- Takei Y, Holtzman B. 2009a. Viscous constitutive relations of solid-liquid composites in terms of grain boundary contiguity: 1. Grain boundary diffusion control model. *J. Geophys. Res.*
- Takei Y, Holtzman B. 2009b. Viscous constitutive relations of solid-liquid composites in terms of grain boundary contiguity: 2. Compositional model for small melt fractions. *J. Geophys. Res.*
- Takei Y, Holtzman B. 2009c. Viscous constitutive relations of solid-liquid composites in terms of grain boundary contiguity: 3. causes and consequences of viscous anisotropy. *J. Geophys. Res.*
- Takei Y, Katz RF. 2015. Consequences of viscous anisotropy in a deforming, two-phase aggregate. Why is porosity-band angle lowered by viscous anisotropy? *J. Fluid Mech.* :199–224
- Tirone M, Sessing J. 2017. Petrological geodynamics of mantle melting i. alphaselts+ multiphase flow: Dynamic equilibrium melting, method and results. *Frontiers in Earth Science* 5:81
- Tolstoy M. 2015. Mid-ocean ridge eruptions as a climate valve. *Geophysical Research Letters*
- Turner S, Bourdon B. 2011. Melt transport from the mantle to the crust—uranium-series isotopes. *Timescales of Magmatic Processes: From Core to Atmosphere* :102–115
- Turner S, Evans P, Hawkesworth C. 2001. Ultrafast Source-to-Surface Movement of Melt at Island Arcs from 226Ra-230Th Systematics. *Science* 292:1363–1366
- Turner S, Reagan M, Vigier N, Bourdon B. 2012. Origins of 210pb-226ra disequilibria in basalts: New insights from the 1978 asal rift eruption. *Geochemistry, Geophysics, Geosystems* 13
- Tweed LEL. 2021. Coupling the thermodynamics, kinetics and geodynamics of multiphase reactive transport in earth’s interior. Ph.D. thesis, Columbia University
- von Bargen N, Waff HS. 1986. Permeabilities, interfacial areas and curvatures of partially molten systems: Results of numerical computations of equilibrium microstructures. *Journal of Geophysical Research: Solid Earth* 91:9261–9276
- Šrámek O, Ricard Y, Bercovici D. 2007. Simultaneous melting and compaction in deformable two-phase media. *Geophysical Journal International* 168:964–982
- Wang S, Constable S, Rychert CA, Harmon N. 2020. A lithosphere-asthenosphere boundary and partial melt estimated using marine magnetotelluric data at the central middle atlantic ridge. *Geochemistry, Geophysics, Geosystems* 21:e2020GC009177
- Wark DA, Watson E. 1998. Grain-scale permeabilities of texturally equilibrated, monomineralic rocks. *Earth and Planetary Science Letters* 164:591–605
- Weatherley SM, Katz RF. 2012. Melting and channelized magmatic flow in chemically heterogeneous, upwelling mantle. *Geochemistry Geophysics Geosystems* 13
- White LT, Rawlinson N, Lister GS, Waldhauser F, Hejrani B, et al. 2019. Earth’s deepest earthquake swarms track fluid ascent beneath nascent arc volcanoes. *Earth and Planetary Science Letters* 521:25–36
- Wilson CR, Spiegelman M, van Keken PE, Hacker BR. 2014. Fluid flow in subduction zones: The role of solid rheology and compaction pressure. *Earth And Planetary Science Letters* 401:261–274
- Yamauchi H, Takei Y. 2016. Polycrystal anelasticity at near-solidus temperatures. *Journal of Geophysical Research: Solid Earth* 121:7790–7820
- Yarushina VM, Podladchikov YY, Connolly JAD. 2015. (De)compaction of porous viscoelastoplastic media: Solitary porosity waves. *Journal Of Geophysical Research-Solid Earth* 120:4843–4862
- Yarushina VM, Podladchikov YY, Wang LH. 2020. Model for (de)compaction and porosity waves in porous rocks under shear stresses. *Journal of Geophysical Research: Solid Earth* 125:e2020JB019683
- Zhang N, Behn MD, Parmentier EM, Kincaid C. 2020. Melt segregation and depletion during ascent of buoyant diapirs in subduction zones. *Journal of Geophysical Research: Solid Earth* 125